

Does the obscured AGN fraction really depend on luminosity?

S. Sazonov^{1*}, E. Churazov^{2,1} and R. Krivonos¹

¹*Space Research Institute, Russian Academy of Sciences, Profsoyuznaya 84/32, 117997 Moscow, Russia*

²*Max-Planck-Institut für Astrophysik, Karl-Schwarzschild-Str. 1, 85740 Garching bei München, Germany*

9 November 2021

ABSTRACT

We use a sample of 151 local non-blazar AGN selected from the *INTEGRAL* all-sky hard X-ray survey to investigate if the observed declining trend of the fraction of obscured (i.e. showing X-ray absorption) AGN with increasing luminosity is mostly an intrinsic or selection effect. Using a torus-obscuration model, we demonstrate that in addition to negative bias, due to absorption in the torus, in finding obscured AGN in hard X-ray flux limited surveys, there is also positive bias in finding unobscured AGN, due to Compton reflection in the torus. These biases can be even stronger taking into account plausible intrinsic collimation of hard X-ray emission along the axis of the obscuring torus. Given the AGN luminosity function, which steepens at high luminosities, these observational biases lead to a decreasing observed fraction of obscured AGN with increasing luminosity even if this fraction has no intrinsic luminosity dependence. We find that if the central hard X-ray source in AGN is isotropic, the intrinsic (i.e. corrected for biases) obscured AGN fraction still shows a declining trend with luminosity, although the intrinsic obscured fraction is significantly larger than the observed one: the actual fraction is larger than $\sim 85\%$ at $L \lesssim 10^{42.5}$ erg s⁻¹ (17–60 keV), and decreases to $\lesssim 60\%$ at $L \gtrsim 10^{44}$ erg s⁻¹. In terms of the half-opening angle θ of an obscuring torus, this implies that $\theta \lesssim 30^\circ$ in lower-luminosity AGN, and $\theta \gtrsim 45^\circ$ in higher-luminosity ones. If, however, the emission from the central SMBH is collimated as $dL/d\Omega \propto \cos \alpha$, the intrinsic dependence of the obscured AGN fraction is consistent with a luminosity-independent torus half-opening angle $\theta \sim 30^\circ$.

Key words: galaxies: active – galaxies: nuclei – galaxies: Seyfert.

1 INTRODUCTION

A lot of recent studies based on X-ray and hard X-ray extragalactic surveys have demonstrated that the fraction of X-ray absorbed (hereafter referred to as obscured) active galactic nuclei (AGN) decreases with increasing observed X-ray luminosity, at least at $\gtrsim 10^{42}$ erg s⁻¹, both in the local ($z \approx 0$) and high-redshift Universe (Ueda et al. 2003; Steffen et al. 2003; Hasinger 2004; Sazonov & Revnivtsev 2004; La Franca et al. 2005; Sazonov et al. 2007; Hasinger 2008; Beckmann et al. 2009; Brightman & Nandra 2011; Burlon et al. 2011; Ueda et al. 2014; Aird et al. 2015; Buchner et al. 2015; note also earlier evidence, Lawrence & Elvis 1982). This might indicate that the opening angle of the (presumably) toroidal obscuring structure – the key element of AGN unification schemes

– increases with AGN luminosity, for example due to feedback of the central supermassive black hole (SMBH) on the accretion flow.

Could the observed luminosity dependence of the obscured AGN fraction arise due to selection effects? This question has been occasionally raised before (e.g. Mayo & Lawrence 2013) and is prompted by the fact that even hard X-ray ($\gtrsim 10$ keV) surveys, which are usually flux (or signal-to-noise ratio) limited, should be biased against detection of Compton-thick AGN, i.e. objects viewed through absorption column density $N_{\text{H}} \gtrsim 10^{24}$ cm⁻², let alone X-ray surveys at energies below 10 keV which must be biased against even Compton-thin obscured sources. Due to this detection bias, the observed fraction of obscured AGN is expected to be lower than the intrinsic fraction of such objects. Furthermore, this effect may depend on luminosity, somehow reflecting the shape of the AGN luminosity function (LF). In fact, as discussed by Lawrence & Elvis (2010), some mid-infrared selected, radio

* E-mail: sazonov@iki.rssi.ru

selected and volume-limited AGN samples do *not* demonstrate any clear luminosity dependence of the proportion of type 1 (i.e. containing broad emission lines in the optical spectrum) and type 2 AGN.

Although there have been previous attempts (Ueda et al. 2003; Malizia et al. 2009; Burlon et al. 2011; Ueda et al. 2014) to take into account detection biases when estimating the space density of obscured AGN based on hard X-ray surveys, they were, in our view, not fully self-consistent and/or used too small samples of hard X-ray selected AGN. It is our goal here to improve on both of these aspects.

The purpose of the present study is to i) evaluate the impact on the observed hard X-ray LF and observed luminosity dependence of the obscured AGN fraction of the *negative bias* for obscured AGN discussed above and a *positive bias* that we demonstrate likely exists for unobscured AGN, and ii) reconstruct the *intrinsic* dependence of the fraction of obscured AGN on luminosity in the local Universe. Our treatment is based on a realistic torus-like obscuration model and makes use of the *INTEGRAL*/IBIS 7-year (2002–2009) hard X-ray survey of the extragalactic sky. Our sample consists of ~ 150 local ($z \lesssim 0.2$) Seyfert galaxies and is highly complete and reliable. Although there are now significantly larger hard X-ray selected samples of local AGN, based on additional observations by *INTEGRAL*/IBIS and especially by *Swift*/BAT, they currently suffer from significant incompleteness as concerns identification and absorption column density information. Most importantly, our sample is large enough to contain a significant number, 17, of heavily obscured ($N_{\text{H}} \geq 10^{24} \text{ cm}^{-2}$) AGN, for which we use as much as possible N_{H} estimates based on high-quality hard X-ray spectral data, in particular from the *NuSTAR* observatory, which has recently been systematically observing AGN discovered in the *Swift*/BAT and *INTEGRAL*/IBIS hard X-ray surveys.

We adopt a Λ CDM cosmological model with $\Omega_{\text{m}} = 0.3$ and $H_0 = 70 \text{ km s}^{-1} \text{ Mpc}^{-3}$.

2 THE INTEGRAL AGN SAMPLE

We use the catalogue of sources (Krivonos et al. 2010b) from the *INTEGRAL*/IBIS 7-year all-sky hard X-ray survey (hereafter, the *INTEGRAL* 7-year survey, Krivonos et al. 2010a). To minimise possible biases in our study of the local AGN population due to remaining unidentified *INTEGRAL* sources and objects with missing distance and/or X-ray absorption information, we exclude from the consideration the Galactic plane region ($|b| < 5^\circ$). The catalogue is composed of sources detected on the time-averaged (December 2002 – July 2009) 17–60 keV map of the sky and is significance limited (5σ). The corresponding flux limit varies over the sky: $f_{\text{det}} < 2.6 \times 10^{-11}$ ($< 7 \times 10^{-11} \text{ erg s}^{-1} \text{ cm}^{-2}$) for 50% (90%) of the extragalactic ($|b| > 5^\circ$) sky (see Fig. 1).

The main properties of the *INTEGRAL* 7-year survey and of the corresponding catalogue of sources were described by Krivonos et al. (2010a,b). Using this catalogue, Sazonov et al. (2010) made preliminary estimates of the hard X-ray LF of local AGN and the dependence of the obscured AGN fraction on luminosity. Subsequent follow-up efforts by different teams have resulted in additional identi-

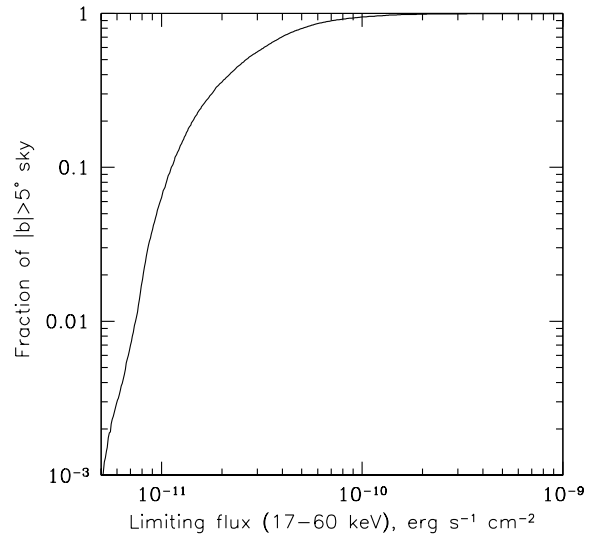


Figure 1. Cumulative fraction of the extragalactic ($|b| > 5^\circ$) sky as a function of flux limit in the *INTEGRAL* 7-year survey.

fications, classifications, distance measurements and X-ray absorption column estimates for many *INTEGRAL* sources, which has significantly improved the quality of the catalogue, as detailed below.

The final sample used here consists of 151 non-blazar (i.e. Seyfert-like) AGN (see Table A1 in Appendix A), with blazars (15 in total) being excluded from the analysis. The sample is highly complete, as there are only 4 sources at $|b| > 5^\circ$ from the *INTEGRAL* 7-year catalogue that remain unidentified. Moreover, all of our AGN have known distances and reliable estimates of their absorption columns based on X-ray spectroscopy. As illustrated in Fig. 2, our sample is mostly local, with 146 out of the 151 objects being located at $z < 0.2$, and spans about 5 decades in (observed) luminosity, from $L_{\text{obs}} \sim 10^{41}$ to $\sim 10^{46} \text{ erg s}^{-1}$ (hereafter, all luminosities are in the 17–60 keV energy band, unless specified otherwise).

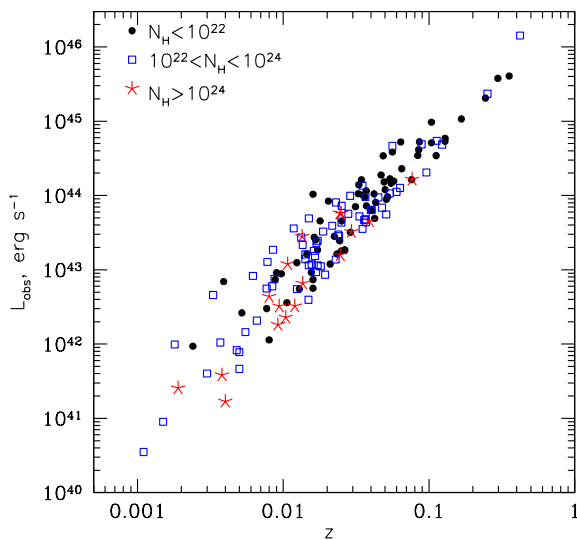
We note that although we used the most up-to-date information from the NASA/IPAC Extragalactic Database (NED) and recent literature to remove blazars from our AGN sample, we cannot rule out that some of our objects have blazar-like properties, i.e. their observed hard X-ray emission contains a significant contribution from a relativistic jet. The most suspicious in this respect are objects classified as broad-line (i.e. presumably oriented towards us) radio galaxies. There are 6 such AGN in our sample: 3C 111, 3C 120, Pic A, 3C 390.3, 4C +74.26 and S5 2116+81. All of them have $L_{\text{obs}} > 10^{44} \text{ erg s}^{-1}$ (but $< 10^{45} \text{ erg s}^{-1}$), i.e. belong to the high-luminosity part of the sample. However, the total number of objects with $L_{\text{obs}} > 10^{44} \text{ erg s}^{-1}$ is much larger: 42. This suggests that possible incomplete filtering of the sample from blazars is unlikely to significantly affect the results and conclusions of this work.

2.1 Absorption columns, heavily obscured AGN

For the purposes of this study it is important to have maximally complete and reliable information on the X-

Table 1. Heavily obscured AGN from the *INTEGRAL* 7-year survey

Object	D Mpc	L_{obs} erg s $^{-1}$	N_{H} cm $^{-2}$	Reference for N_{H}
SWIFT J0025.8+6818	52.0	3.2×10^{42}	$> 10^{25}$	<i>NuSTAR</i> (Krivonos et al. 2015)
NGC 1068	12.3	3.8×10^{41}	$> 10^{25}$	<i>NuSTAR</i> (Bauer et al. 2014)
NGC 1194	59.0	6.6×10^{42}	$\sim 10^{24}?$	<i>XMM-Newton</i> (below 10 keV, Greenhill, Tilak, & Madejski 2008)
CGCG 420-015	129.2	3.3×10^{43}	$> 10^{25}$	<i>NuSTAR</i> (Krivonos et al. 2015)
MRK 3	58.6	2.8×10^{43}	10^{24}	<i>Suzaku</i> (Ikeda, Awaki, & Terashima 2009)
IGR J09253+6929	172.6	4.5×10^{43}	$> 10^{24}?$	low X-ray/hard X-ray flux ratio (<i>Swift</i> /XRT+ <i>INTEGRAL</i> /IBIS)
NGC 3081	28.6	4.4×10^{42}	10^{24}	<i>Suzaku</i> (Eguchi et al. 2011)
NGC 3281	46.3	1.2×10^{43}	2×10^{24}	<i>BeppoSAX</i> (Vignali & Comastri 2002)
ESO 506-G027	109.5	5.8×10^{43}	10^{24}	<i>Suzaku</i> (Winter et al. 2009b)
NGC 4939	34.7	2.3×10^{42}	$> 10^{25}?$	<i>BeppoSAX</i> (Maiolino et al. 1998), but varied to $N_{\text{H}} = 1.5 \times 10^{23}$ cm $^{-2}$ (<i>XMM-Newton</i> , below 10 keV, Guainazzi et al. 2005a)
NGC 4945	3.4	2.6×10^{41}	4×10^{24}	<i>NuSTAR</i> (Puccetti et al. 2014; Brightman et al. 2015), <i>Suzaku</i> (Yaqoob 2012)
IGR J14175–4641	348.3	1.6×10^{44}	$> 10^{24}?$	low X-ray/hard X-ray flux ratio (<i>Swift</i> /XRT+ <i>INTEGRAL</i> /IBIS)
NGC 5643	11.8	1.7×10^{41}	$> 10^{25}$	<i>NuSTAR</i> (Krivonos et al. 2015)
NGC 5728	24.8	3.2×10^{42}	2×10^{24}	<i>NuSTAR</i> (Krivonos et al. 2015)
IGR J14561–3738	107.7	1.6×10^{43}	$\sim 10^{24}$	<i>Chandra</i> + <i>INTEGRAL</i> /IBIS (Sazonov et al. 2008)
ESO 137-G034	33.0	1.8×10^{42}	$> 10^{25}$	<i>Suzaku</i> (Comastri et al. 2010)
NGC 6240	107.3	5.8×10^{43}	2.5×10^{24}	<i>NuSTAR</i> (Krivonos et al. 2015)


Figure 2. Observed hard X-ray (17–60 keV) luminosity vs. redshift for non-blazar AGN from the *INTEGRAL* 7-year survey. Filled circles, empty squares and stars denote unobscured, lightly obscured and heavily obscured objects, respectively.

ray absorption columns, N_{H} , of the studied AGN. Our starting source of such information is our previous papers on the *INTEGRAL*/IBIS survey (Sazonov et al. 2007, 2012) as well as on the *RXTE* (3–20 keV) slew survey (Sazonov & Revnivtsev 2004), but we have updated the N_{H} estimates in all cases where it was necessary and possible (see Table A1).

For unobscured and lightly obscured ($N_{\text{H}} < 10^{24}$ cm $^{-2}$) sources, X-ray spectroscopy at energies below 10 keV is usually sufficient for evaluating N_{H} . Such data do exist for all of our sources and in most cases there are reliable published N_{H} values, which we adopt. Furthermore, if the absorption

column is less than 10^{22} cm $^{-2}$, we adopt $N_{\text{H}} = 0$ and consider such sources unobscured.

However, absorption column estimates based on X-ray data below 10 keV become unreliable for strongly absorbed sources, having $N_{\text{H}} \geq 10^{24}$ cm $^{-2}$. In such cases, we prefer to use results from hard X-ray (above 10 keV) spectroscopy, whenever possible. Specifically, our preference list of instruments is headed by *NuSTAR* – the unique focusing hard X-ray telescope, followed by *Suzaku* and then by all other currently operating or previously flown hard X-ray missions.

For five of the heavily obscured ($N_{\text{H}} \geq 10^{24}$ cm $^{-2}$) objects and candidates, we carried out our own analysis of publicly available *NuSTAR* data (Krivonos et al. 2015). Specifically, we fitted the spectra by a sum of a strongly absorbed power-law component (with a high-energy cutoff) and a disk-reflection continuum modelled with *pevrv* in XSPEC. The *NuSTAR* spectra of SWIFT J0025.8+6818, CGCG 420-015 and NGC 5643 are consistent with being fully reflection dominated (i.e. dominated by Compton-scattered continuum), and so we prescribed $N_{\text{H}} > 10^{25}$ cm $^{-2}$ to them. The other two objects, NGC 5728 and NGC 6240, along with strong reflection demonstrate a significant contribution from the primary component suppressed by intrinsic absorption at the level of $N_{\text{H}} \sim 2\text{--}2.5 \times 10^{24}$ cm $^{-2}$. More physically motivated AGN torus models confirmed this qualitative result (see Krivonos et al. 2015 for details). Our derived spectral parameters for CGCG 420-015, NGC 5643, NGC 5728 and NGC 6240 are consistent with pre-*NuSTAR* estimates for these objects (Severgnini et al. 2011, Matt et al. 2013, Comastri et al. 2010, Vignati et al. 1999, respectively).

In total, our sample consists of 67 unobscured ($N_{\text{H}} < 10^{22}$ cm $^{-2}$) and 84 obscured ($N_{\text{H}} \geq 10^{22}$ cm $^{-2}$) AGN, including 17 heavily obscured ($N_{\text{H}} \geq 10^{24}$ cm $^{-2}$) ones.

Table 1 provides key information about our heavily obscured AGN. For 7 of these, there are reliable N_{H} estimates or evidence that the source’s spectrum is reflection-dominated (in which case we adopt that $N_{\text{H}} > 10^{25}$ cm $^{-2}$) from *NuSTAR* observations. All but one (IGR J14561–3738) of the remaining 10 objects are either

planned to be observed by *NuSTAR* soon or have already been observed by this telescope but the data are proprietary at the time of writing. However, for most of these sources there exists fairly reliable information from other hard X-ray missions indicating that $N_{\text{H}} \geq 10^{24} \text{ cm}^{-2}$ – see Table 1.

Three of the objects included in our sample of heavily obscured AGN are currently candidates rather than firmly established representatives of this class: the quoted value $N_{\text{H}} \sim 10^{24} \text{ cm}^{-2}$ for NGC 1194 comes from X-ray data below 10 keV, whereas the presence of $N_{\text{H}} > 10^{24} \text{ cm}^{-2}$ absorption columns in IGR J09253+6929 and IGR J14175–4641 is strongly suggested by very low ($\lesssim 0.01$) X-ray/hard X-ray flux ratios that we find for them from *Swift*/XRT and *INTEGRAL*/IBIS data. Note that we initially used the same argument to regard another source from this sample, SWIFT J0025.8+6818, as a likely heavily obscured AGN, and it indeed proved to be such once we analysed *NuSTAR* data. In the analysis below, we assume that $N_{\text{H}} = 3 \times 10^{24} \text{ cm}^{-2}$ for both IGR J09253+6929 and IGR J14175–4641.

The most difficult case is that of NGC 4939, which manifested itself as a reflection-dominated source ($N_{\text{H}} > 10^{25} \text{ cm}^{-2}$) during *BeppoSAX* observations in 1997 (Maiolino et al. 1998), but was found to be in a Compton-thin state, with $N_{\text{H}} \sim 1.5 \times 10^{23} \text{ cm}^{-2}$, by *XMM-Newton* in 2001 (Guainazzi et al. 2005a). We nevertheless treat NGC 4939 as a reflection-dominated source in our analysis, in part because the hard X-ray flux measured by *INTEGRAL* for this source is similar to that measured by *BeppoSAX* but lower than the flux inferred from the *XMM-Newton* observation and so *INTEGRAL* may have caught the source in a state similar to that revealed by *BeppoSAX*. Generally, we adopt $N_{\text{H}} = 10^{25} \text{ cm}^{-2}$ for reflection-dominated sources (there are in total 6 such objects) in our analysis, although in reality the column density in such objects may be even higher, say $N_{\text{H}} \sim 10^{26} \text{ cm}^{-2}$.

We have thus obtained a fairly large and high-quality (in terms of information on intrinsic obscuration) sample of heavily obscured AGN. The high completeness and reliability of this sample are crucial for our analysis below.

3 OBSERVED PROPERTIES OF LOCAL AGN

We first consider a number of *observed* properties of the local AGN population using our *INTEGRAL* sample.

Fig. 3 shows the observed distribution of absorption columns for our objects, while Fig. 4 shows the observed dependence of the obscured AGN fraction on hard X-ray luminosity. The latter was obtained by counting obscured and unobscured sources within specified luminosity bins and dividing the first number by the sum of the two. One can clearly see a declining trend of the obscured AGN fraction with increasing luminosity, which is well known from previous studies.

We next calculated the observed hard X-ray LF, $\phi(L_{\text{obs}})$ (number of objects per Mpc^3 per $\log L_{\text{obs}}$), of local AGN: both in binned and analytic form (see Fig. 5). The analytic LF model used throughout this study is a broken power law:

$$\frac{dN_{\text{AGN}}}{d \log L} = \frac{A}{(L/L_*)^{\gamma_1} + (L/L_*)^{\gamma_2}}. \quad (1)$$

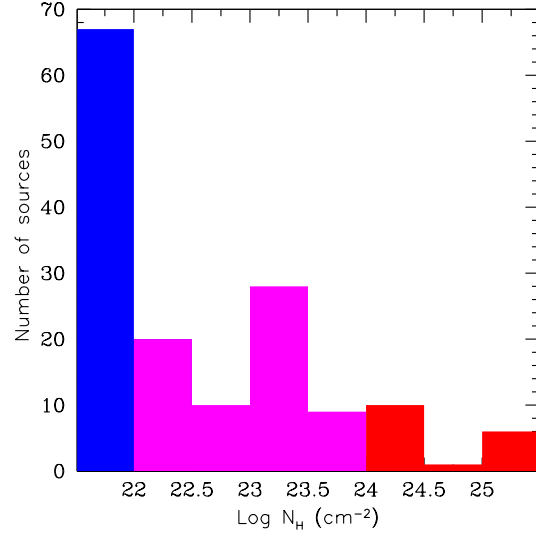


Figure 3. Observed distribution of X-ray absorption columns for the *INTEGRAL* AGN. Unobscured ($N_{\text{H}} < 10^{22} \text{ cm}^{-2}$), lightly obscured ($10^{22} \leq N_{\text{H}} < 10^{24} \text{ cm}^{-2}$) and heavily obscured ($N_{\text{H}} \geq 10^{24} \text{ cm}^{-2}$) objects are shown in blue, magenta and red, respectively.

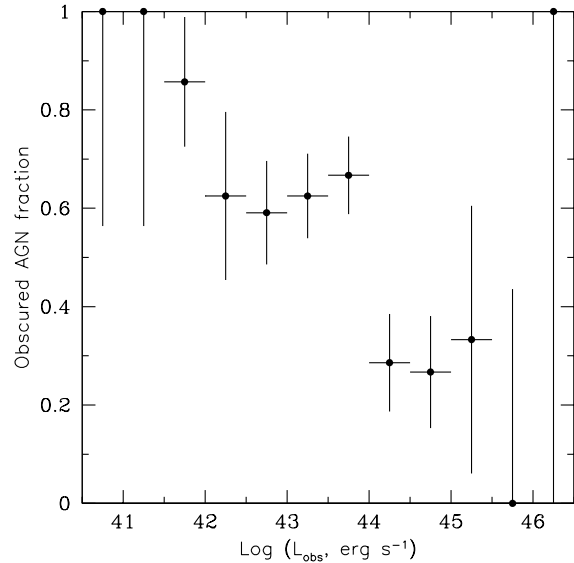


Figure 4. Observed fraction of obscured ($N_{\text{H}} \geq 10^{22} \text{ cm}^{-2}$) AGN as a function of observed hard X-ray luminosity for the *INTEGRAL* 7-year survey.

The binned LF was constructed using the standard $1/V_{\text{max}}$ method, whereas the best-fit values (and their uncertainties) of the characteristic luminosity, L_* , and of the two slopes, γ_1 and γ_2 , of the analytic model (see Table 2) were found using a maximum likelihood estimator (similarly to Sazonov et al. 2007):

$$\mathcal{L} = -2 \sum_i \ln \frac{\phi(L_{\text{obs},i}) V_{\text{max}}(L_{\text{obs},i})}{\int \phi(L_{\text{obs}}) V_{\text{max}}(L_{\text{obs}}) d \log L_{\text{obs}}}, \quad (2)$$

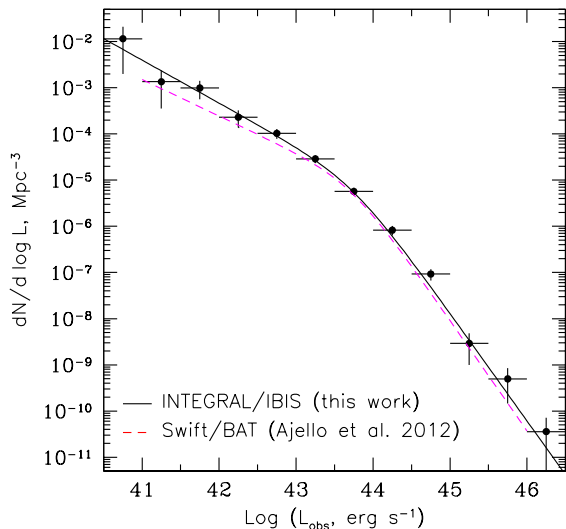


Figure 5. Observed (in the *INTEGRAL* 7-year survey) hard X-ray luminosity function of local AGN (filled circles) fitted by a broken power law (black solid line). The best-fit parameters are given in Table 2. For comparison the LF based on the *Swift*/BAT survey (Ajello et al. 2012) is shown by the magenta dashed line.

where $L_{\text{obs},i}$ are the observed luminosities of AGN in our sample, and $V_{\text{max}}(L_{\text{obs}})$ is the volume of the Universe probed by the *INTEGRAL* 7-year survey for a given L_{obs} , which can be calculated from the sky coverage curve (see Fig. 1). The normalization of the analytic model is derived from the actual number of objects in the sample.

Comparing this newly determined observed hard X-ray LF with our old result (Sazonov et al. 2007) based on a smaller set (66 vs. 151 objects) of AGN detected with *INTEGRAL*, we find good agreement between the two, but the constraints on the LF parameters have now significantly improved. We can also compare the *INTEGRAL* LF with that derived from a still larger (361 objects) sample of (mostly) local AGN found in nearly the same energy band (15–55 keV) in the *Swift*/BAT survey (Ajello et al. 2012). As can be seen in Fig. 5, the two LFs are in good agreement with each other.

Finally, we calculated separately the observed LFs of unobscured and obscured AGN (see Fig. 6). It can be seen that these LFs are different in shape, as is verified by the best-fit parameters of the corresponding analytic fits (see Table 2).

4 INTRINSIC PROPERTIES OF LOCAL AGN

The observed LF just discussed has not been corrected for any effects associated with absorption or scattering of hard X-rays emitted by the AGN central source on the way between the source and the observer, nor for any intrinsic anisotropy of the emission generated by the central source in AGN. This observed LF is expected to be affected by absorption bias: an obscured AGN will be inferred to have a lower luminosity, $L_{\text{obs}} = f_{\text{obs}} \times 4\pi D^2$ (here, f_{obs} is the measured hard X-ray flux and D is the distance to the source), than

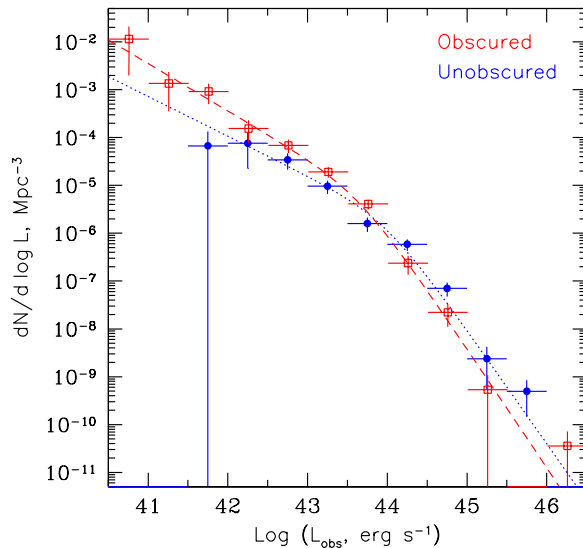


Figure 6. Observed hard X-ray luminosity functions of unobscured ($N_{\text{H}} < 10^{22} \text{ cm}^{-2}$, blue filled circles) and obscured ($N_{\text{H}} \geq 10^{22} \text{ cm}^{-2}$, red empty squares) AGN, fitted by broken power laws (blue dotted and red dashed lines, respectively). The best-fit parameters are given in Table 2.

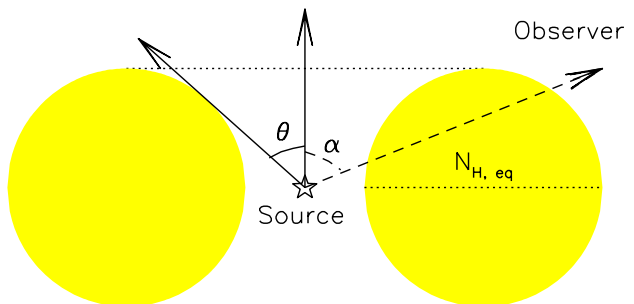


Figure 7. Torus model.

its intrinsic (i.e. emitted by the central source) luminosity, L_{intr} , and a source like this can be found in a flux-limited hard X-ray survey within a smaller volume of the Universe than it would be in the absence of X-ray absorption: $V_{\text{max}}(L_{\text{obs}})/V_{\text{max}}(L_{\text{intr}}) \approx (L_{\text{obs}}/L_{\text{intr}})^{3/2}$. Here, the approximation symbol reflects the fact that AGN obscuration may also affect the shape of the measured X-ray spectrum and thus the number of photons recorded by a given detector with its specific energy response. On the other hand, as discussed below, unobscured AGN are expected to have higher observed luminosities than their intrinsic angular-averaged luminosities and can thus be detected within a larger V_{max} . We can correct for both of these biases and obtain an intrinsic hard X-ray LF of local AGN. To this end, we use a physically motivated obscuration model described below.

Table 2. Fits of different hard X-ray luminosity functions by a broken power law

AGN class	N_{AGN}	$\log L_*$	γ_1	γ_2	A^a , 10^{-5} Mpc^{-3}	Num. density ($\log L = 40.5\text{--}46.5$) 10^{-4} Mpc^{-3}	Lum. density ($\log L = 40.5\text{--}46.5$) $10^{39} \text{ erg s}^{-1} \text{ Mpc}^{-3}$
Observed LF							
All	151	43.74 ± 0.19	0.93 ± 0.10	2.33 ± 0.15	1.122	54 (41 ÷ 82)	1.57 ± 0.20
Unobscured	67	43.98 ± 0.32	0.83 ± 0.18	2.37 ± 0.28	0.243	10 (7 ÷ 25)	0.45 ± 0.08
Obscured	84	43.65 ± 0.21	0.99 ± 0.21	2.48 ± 0.22	0.839	48 (37 ÷ 78)	1.14 ± 0.18
Intrinsic LF, isotropic emission, $\theta = 30^\circ$							
All	151	43.69 ± 0.18	0.89 ± 0.10	2.36 ± 0.16	1.806	61 (47 ÷ 96)	1.97 ± 0.25
Unobscured	67	43.87 ± 0.31	0.84 ± 0.18	2.39 ± 0.28	0.201	7.0 (5.1 ÷ 16.7)	0.30 ± 0.05
Obscured	84	43.62 ± 0.21	0.93 ± 0.12	2.45 ± 0.21	1.581	59 (46 ÷ 101)	1.63 ± 0.26
Intrinsic LF, isotropic emission, $\theta = 45^\circ$							
All	151	43.71 ± 0.19	0.89 ± 0.10	2.36 ± 0.16	1.494	52 (41 ÷ 82)	1.71 ± 0.21
Unobscured	67	43.90 ± 0.31	0.84 ± 0.18	2.39 ± 0.27	0.203	7.5 (5.4 ÷ 18.2)	0.32 ± 0.06
Obscured	84	43.62 ± 0.21	0.92 ± 0.12	2.44 ± 0.21	1.698	59 (46 ÷ 105)	1.70 ± 0.26
Intrinsic LF, cosine-law emission, $\theta = 30^\circ$							
All	151	43.69 ± 0.17	0.90 ± 0.10	2.43 ± 0.17	1.593	57 (44 ÷ 87)	1.79 ± 0.21
Unobscured	67	43.70 ± 0.30	0.86 ± 0.17	2.42 ± 0.28	0.188	5.3 (3.9 ÷ 11.6)	0.19 ± 0.03
Obscured	84	43.68 ± 0.21	0.93 ± 0.12	2.45 ± 0.21	1.565	66 (51 ÷ 114)	1.88 ± 0.30

^a The normalization A is given without an error because this parameter is strongly correlated with the others.

4.1 Torus model and AGN spectra

We have developed a Monte-Carlo code for modelling AGN X-ray spectra modified by reprocessing in a toroidal structure of gas. The adopted geometry (see Fig. 7) is similar to that used in other existing models, e.g. Ikeda, Awaki, & Terashima (2009); Murphy & Yaqoob (2009); Brightman & Nandra (2011). The key assumptions of our model are:

- (i) The geometrical shape is that of a ring torus;
- (ii) The gas is homogeneous, cold, neutral and of normal cosmic chemical composition;
- (iii) The X-ray spectrum emitted by the central source is a power law with an exponential cutoff, $dN/dE \propto E^{-\Gamma} e^{-E/E_{\text{cut}}}$, with $\Gamma = 1.8$ and $E_{\text{cut}} = 200$ keV;
- (iv) The central (point-like) source is either isotropic, $dL_{\text{intr}}/d\Omega = \text{const}$ – hereafter, Model A, or emitting according to Lambert’s law, $dL_{\text{intr}}/d\Omega \propto \cos \alpha$, where α is the viewing angle with respect to the axis of the torus – hereafter, Model B.

The introduction of Model B is an important aspect of the present study and is motivated by the common belief that the hard X-ray emission observed from AGN is produced by Comptonization of softer emission from an accretion disk around a SMBH in a hot corona lying above the disk. If such a corona has quasi-planar geometry, the hard X-ray flux it produces will be collimated along the axis of the disk/corona roughly as $F \propto \mu$ (the exact law being dependent on the photon energy and the optical depth of the corona, Pozdnyakov, Sobol, & Sunyaev 1983; Sunyaev & Titarchuk 1985), where μ is the cosine of the angle between the outgoing direction and the axis of the disk/corona. Because the obscuring torus in turn is likely coaligned with the accretion disk, the emergent hard X-ray radiation will be collimated along the axis of the torus. In reality, a significant fraction of the coronal emission is reflected by the underlying accretion disk, but this also occurs preferentially along the axis of the disk/torus

(Magdziarz & Zdziarski 1995). Since there is still significant uncertainty in the overall physical picture, we introduce a simple, energy independent collimation factor $dL_{\text{intr}}/d\Omega \propto \cos \alpha$ to get an idea of how strongly intrinsic collimation of hard X-ray emission can affect observed properties of local AGN.

Apart from the two alternatives for the angular dependence of intrinsic emission (Model A or Model B), our model has three free parameters: (i) the equatorial column density, $N_{\text{H,eq}}$ (the total number of H atoms per cm^2 along an equatorial line of sight between the central source and the observer), (ii) half-opening angle of the torus, θ , and (iii) the viewing angle relative to the axis of the torus, α (see Fig. 7).

X-ray photons emitted by the central source can scatter multiple times within the torus before they either get photoabsorbed in the gas or escape from the system. Our radiative transfer calculations are based on a method developed by Churazov et al. (2008). The gas in the torus is assumed to be neutral, with the relative abundances of all elements as in the Solar photosphere. The following processes are included in the simulations: photoelectric absorption, Rayleigh and Compton scattering and fluorescence. Photoelectric absorption is calculated using the data and approximations of Verner & Yakovlev (1995) and Verner et al. (1996). For fluorescence we use the energies and yields from Kaastra & Mewe (1993). Compton and Rayleigh scattering are modelled using differential cross sections provided by the GLECS package (Kippen 2004) of the GEANT code (Agostinelli et al. 2003). Namely, the Livermore Evaluated Photon Data Library (EPDL, see Cullen et al. 1990) and the Klein-Nishina formula for free electrons are used to calculate total cross-sections and the angular distribution of scattered photons for each element.

Figure 8 shows examples of emergent AGN spectra simulated using our model of the obscuring torus. As expected, for obscured AGN ($\alpha > \theta$), the observed hard X-ray flux can be strongly attenuated relative to the emitted flux and for high absorption columns ($N_{\text{H}} \gg 10^{24} \text{ cm}^{-2}$) the spectrum can become reflection-dominated, as the observer will mostly

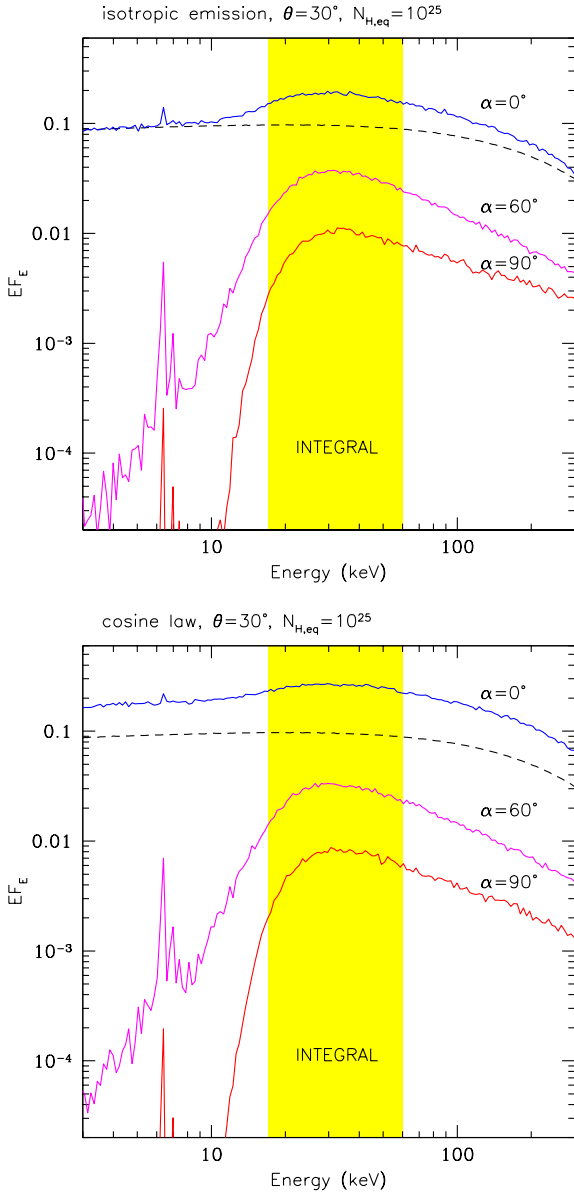


Figure 8. *Top:* Examples of simulated AGN spectra for Model A, half-opening torus angle $\theta = 30^\circ$ and equatorial column density $N_{\text{H,eq}} = 10^{25} \text{ cm}^{-2}$, for various viewing angles. The dashed curve shows the intrinsic (angular-averaged) spectrum. The shaded area indicates the *INTEGRAL*/IBIS energy band used for AGN selection in this work. *Bottom:* The same, but for Model B.

see emission reflected from the inner walls of the torus rather than emission from the central source transmitted through the torus. In this last case, there also appear strong iron $K\alpha$ and $K\beta$ fluorescent lines at 6.4 keV and 7.06 keV. These spectral properties and trends for heavily obscured AGN are of course well known.

We further see from Fig. 8 that the spectra observed from directions $\alpha < \theta$, corresponding to unobscured AGN, also differ from the intrinsic spectrum. Namely, they have an excess due to Compton reflection of hard X-rays from the torus in the direction of the observer. This hump is located approximately within the energy band of 17–60 keV that we

use for detecting AGN in the *INTEGRAL* survey. It is obvious that this Compton reflection component should bias observed luminosities of unobscured AGN higher in this and similar (e.g. *Swift*/BAT) hard X-ray surveys. Any intrinsic collimation of emission along the axis of the obscuring torus will make this positive bias even stronger (see the spectrum for Model B and $\alpha \approx 0$ in the lower panel of Fig. 8). This important aspect is frequently overlooked in AGN population studies, even though a reflection component is well known to be present in the hard X-ray spectra of unobscured AGN.

4.2 AGN detection bias

To quantify biases affecting detection of unobscured and obscured AGN in the *INTEGRAL* survey, we show in Fig. 9, for Model A and Model B, the ratio, $R(N_{\text{H,eq}}, \theta, \alpha) = L_{\text{obs}}/L_{\text{intr}}$, of the observed to intrinsic luminosity in the 17–60 keV energy band as a function of $N_{\text{H,eq}}$, for a torus half-opening angle $\theta = 30^\circ$ and several narrow ranges of the viewing angle α . One can see that R is always larger than unity, i.e. $L_{\text{obs}} > L_{\text{intr}}$, for unobscured AGN. For example, for Model A and $\alpha \approx 0$, R increases from 1 to ~ 2 as $N_{\text{H,eq}}$ increases to a few 10^{24} cm^{-2} and remains at approximately this level thereafter. This trend can be easily understood: the amplitude of Compton reflection is expected to be proportional to the torus optical depth, τ , in the optically thin regime ($\tau \ll 1$) and constant in the opposite case ($\tau \gg 1$). As regards obscured AGN ($\alpha > \theta$), R decreases with increasing $N_{\text{H,eq}}$ and increasing α (apart from a local maximum at $N_{\text{H,eq}} \sim 3 \times 10^{24} \text{ cm}^{-2}$ at near-equatorial directions for Model B – due to the reflected component), as could be expected due to the increasing attenuation of the transmitted component. The most obvious and important difference of Model B with respect to Model A is that the observed hard X-ray flux is anisotropic even in the absence of an obscuring torus (i.e. for $N_{\text{H}} = 0$) – just due to the initial collimation of emission.

We can proceed further and ask the question: what would be the *average* observed/intrinsic flux ratio for the local populations of unobscured and obscured AGN if (i) AGN tori were randomly oriented with respect to the observer, which is a natural assumption, and (ii) all the tori had the same half-opening angle θ (this, of course, permits the physical size of the torus to vary from one object to another and e.g. to depend on luminosity). To this end, we just need to average the dependencies shown in Fig. 9 over the viewing angle α for the unobscured and obscured directions:

$$R_{\text{unobsc}}(N_{\text{H,eq}}, \theta) = \frac{\int_{\cos \theta}^1 R(N_{\text{H,eq}}, \theta, \alpha) d \cos \alpha}{1 - \cos \theta}, \quad (3)$$

$$R_{\text{obsc}}(N_{\text{H,eq}}, \theta) = \frac{\int_0^{\cos \theta} R(N_{\text{H,eq}}, \theta, \alpha) d \cos \alpha}{\cos \theta}. \quad (4)$$

The result is shown in Fig. 10 as a function of $N_{\text{H,eq}}$ for torus half-opening angles $\theta = 30^\circ, 45^\circ$ and 60° . One can see that for Model A, R_{unobsc} (the average observed/intrinsic flux ratio for unobscured AGN) reaches a maximum of ~ 1.5 – 2 , depending on θ , at $N_{\text{H,eq}} \sim 5 \times 10^{24} \text{ cm}^{-2}$, then declines to ~ 1.4 – 1.7 by $N_{\text{H,eq}} \sim 1.5 \times 10^{25} \text{ cm}^{-2}$ and stays at approximately this level for higher column densities. The average ratio R_{obsc} for obscured AGN monotonically decreases from 1 to ~ 0.2 as $N_{\text{H,eq}}$ increases from $\ll 10^{24} \text{ cm}^{-2}$ to

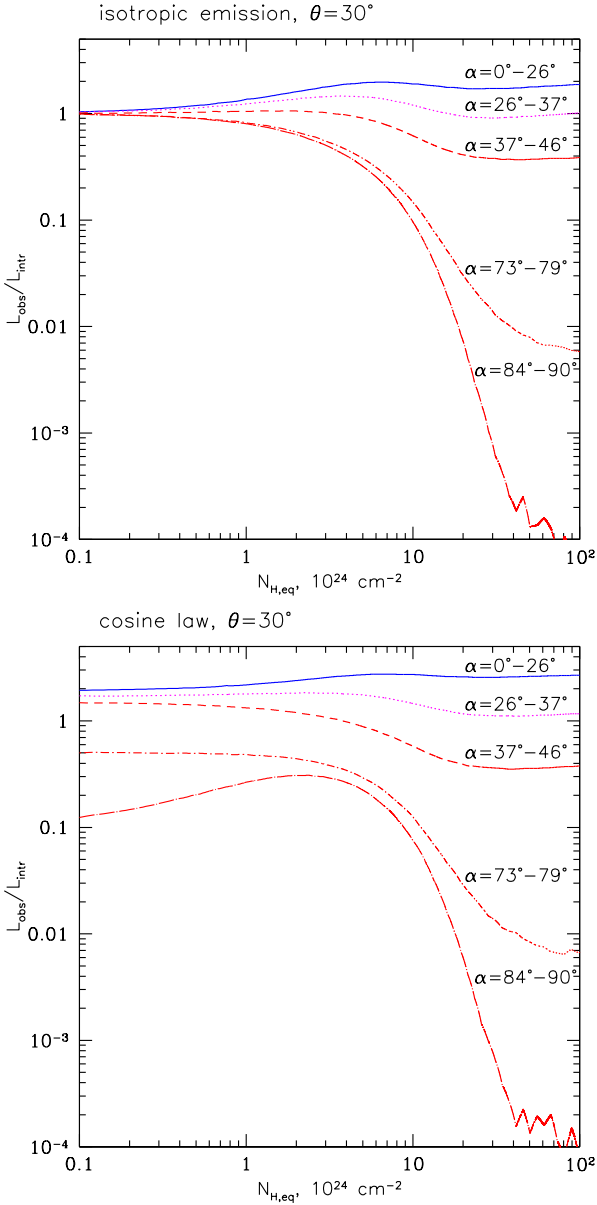


Figure 9. *Top:* Calculated ratio of observed to intrinsic (angular-averaged) luminosity in the 17–60 keV energy band for a torus half-opening angle $\theta = 30^\circ$, for different viewing angles (α), as a function of the torus column density for Model A. *Bottom:* The same, but for Model B.

$\sim 1.5 \times 10^{25} \text{ cm}^{-2}$ and stays at this level thereafter. In the case of a cosine-law emitting source, the situation is qualitatively similar, but the contrast between the unobscured and obscured directions is more pronounced: it is present already at $N_{\text{H}} = 0$ and increases further, due to Compton reflection, with increasing N_{H} .

It is obvious from Fig. 10 that a hard X-ray survey, like the ones performed by *INTEGRAL* and *Swift*, will find unobscured AGN more easily than even lightly obscured objects, let alone heavily obscured ones. Our goal now is to correct the observed statistical properties of local AGN for this obvious bias.

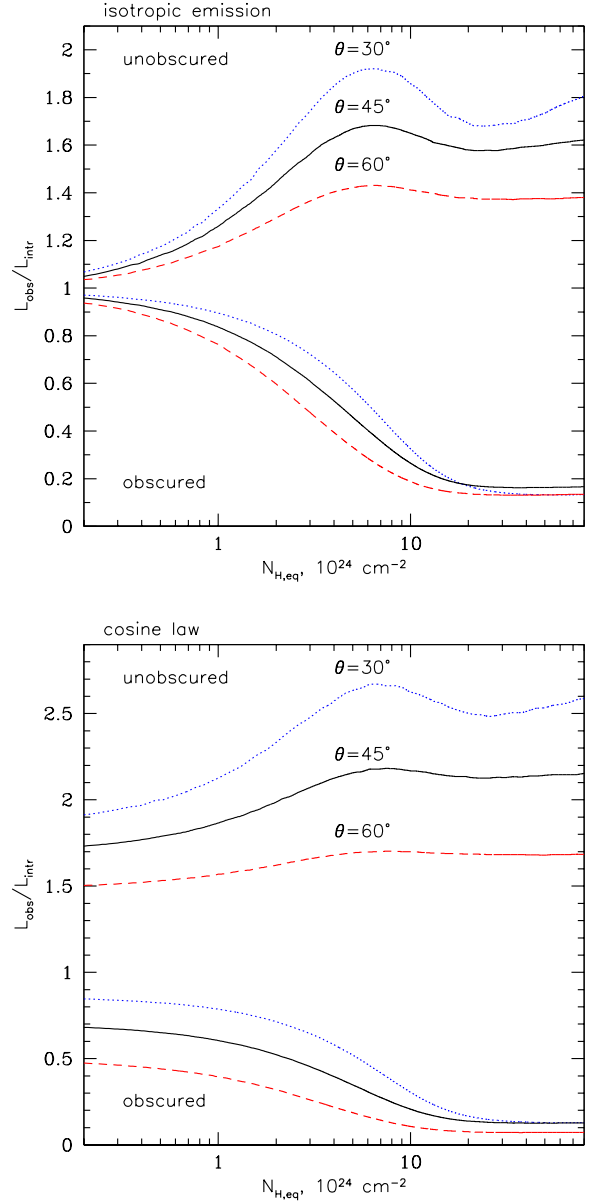


Figure 10. *Top:* Calculated ratio of observed to intrinsic (angular-averaged) luminosity in the 17–60 keV energy band averaged separately over all unobscured and obscured directions ($\alpha < \theta$ and $\alpha > \theta$, respectively) for three values of the torus half-opening angle, as a function of the torus column density, for Model A. *Bottom:* The same, but for Model B.

4.3 Intrinsic distribution of torus column densities

We can first estimate the intrinsic distribution of the column densities, $N_{\text{H,eq}}$, of AGN torii. To this end, we need to correct the observed N_{H} distribution (Fig. 3) for absorption bias, excluding from the consideration the first, $N_{\text{H}} < 10^{22} \text{ cm}^{-2}$, bin since it pertains to unobscured AGN for which our line of sight does not cross the torus. Given the fairly small number of obscured AGN, especially of heavily obscured ones, in our sample, we are bound to make some simplifying assumptions. For example, we may assume that the intrinsic $N_{\text{H,eq}}$ distribution does not depend

on luminosity. In this case, the intrinsic $N_{\text{H,eq}}$ distribution can be estimated simply by dividing the observed one by $R_{\text{obsc}}^{3/2}(N_{\text{H,eq}}, \theta)$ (and normalising the resulting dependence so that its integral over N_{H} equals unity), with the bias factor $R_{\text{obsc}} = L_{\text{obs}}/L_{\text{intr}}$ having been discussed in §4.2.

In doing this exercise, we assumed that $N_{\text{H,eq}} = (4/\pi)N_{\text{H}} \approx 1.27N_{\text{H}}$ for our obscured AGN. This is because we do not know the orientation of our objects apart from the fact that some of them are unobscured and hence $\alpha < \theta$, while others are obscured and hence $\alpha > \theta$. For our assumed torus geometry (see Fig. 7), the line-of-sight column density depends on the viewing angle as follows:

$$N_{\text{H}}(\alpha) = N_{\text{H,eq}} \sqrt{1 - \left(\frac{\cos \alpha}{\cos \theta}\right)^2}, \quad (5)$$

so that the mean N_{H} over all obscured directions is

$$N_{\text{H,obsc}} = \frac{\int_0^{\cos \theta} N_{\text{H}}(\alpha) d \cos \alpha}{\cos \theta} = \frac{\pi}{4} N_{\text{H,eq}}. \quad (6)$$

Hence the coefficient in the conversion of N_{H} to $N_{\text{H,eq}}$ above. Note that the N_{H} values adopted from the literature for some of our Compton-thick AGN may already have been ascribed the meaning of an equatorial rather than line-of-sight column density by the corresponding authors. However, considering our sample of heavily obscured sources as a whole, the information it contains on the absorption columns is very heterogeneous, as it is based on various spectral models used by various authors. Fortunately, a typical expected difference between $N_{\text{H,eq}}$ and N_{H} for obscured AGN is only $\sim 20\%$ (see equation (6) above) and has negligible impact on our results.

The resulting intrinsic $N_{\text{H,eq}}$ distribution is presented in Fig. 11. It is only weakly dependent on both the assumed half-opening angle θ of the obscuring torus and the assumed emission model (Model A or Model B). This distribution can be roughly described as log-uniform between $N_{\text{H,eq}} = 10^{22}$ and 10^{26} cm^{-2} , although the upper boundary is, of course, fairly uncertain. A similar result was previously obtained using AGN from the *Swift*/BAT hard X-ray survey (Burlon et al. 2011; Ueda et al. 2014). Moreover, the intrinsic N_{H} distribution shown in Fig. 11 is similar to the one inferred for optically selected Seyfert 2 galaxies (Risaliti, Maiolino, & Salvati 1999).

4.4 Intrinsic luminosity function

We now calculate the intrinsic hard X-ray LF of unobscured and obscured AGN, $\phi(L_{\text{intr}}) \equiv dN/d \log L_{\text{intr}}$. As for the observed LFs discussed in §3, we use both binned and analytic representations.

For the binned LFs, the procedure is as follows:

(i) First, based on the observed luminosity $L_{\text{obs},i}$ and estimated torus column density $N_{\text{H,eq},i}$ of each source in the sample (Table A1), we determine its intrinsic hard X-ray luminosity as either $L_{\text{intr},i} = L_{\text{obs},i}/R_{\text{unobsc}}(N_{\text{H,eq},i}, \theta)$ (for unobscured sources) or $L_{\text{intr},i} = L_{\text{obs},i}/R_{\text{obsc}}(N_{\text{H,eq},i}, \theta)$ (for obscured sources), where the ratios R_{unobsc} and R_{obsc} are calculated as discussed above (from eqs. (3) and (4), see Fig. 10), assuming some (the same for all objects) torus half-opening angle θ and using Model A or Model B. Here again we use the average ratios R_{unobsc} and R_{obsc} rather

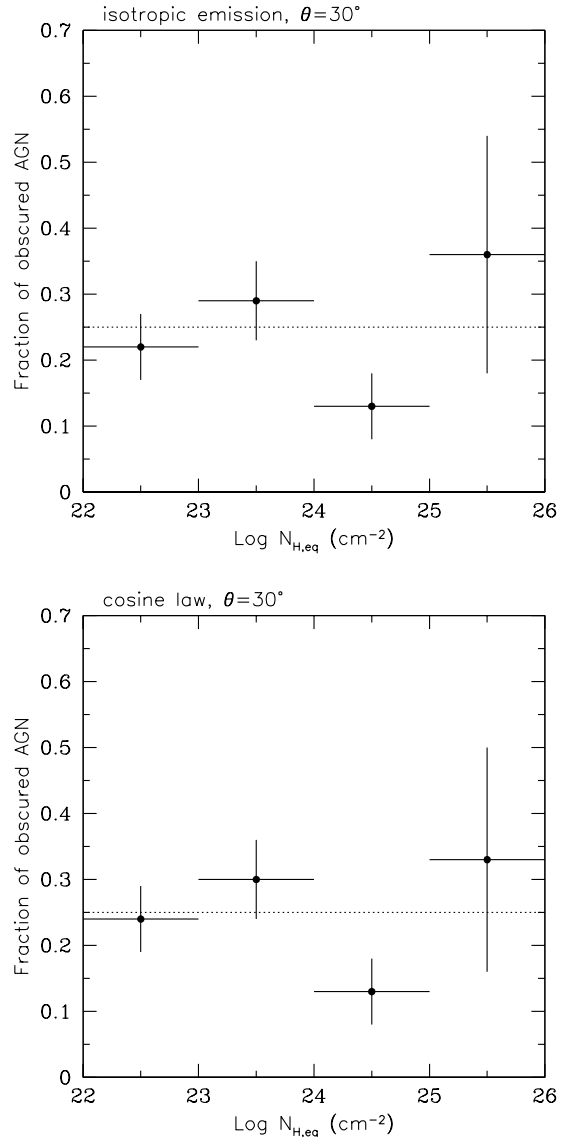


Figure 11. Reconstructed intrinsic distribution of column densities of obscuring tori in local AGN, calculated assuming $\theta = 30^\circ$ and either Model A (top) or Model B (bottom). The dotted line corresponds to a log-uniform distribution.

than the viewing-angle dependent $R(N_{\text{H,eq}}, \theta, \alpha)$ from which they derive for the lack of knowledge of the orientation of our objects. Strictly speaking, this procedure is not fully correct, because for given $N_{\text{H,eq}}$ and θ , a hard X-ray flux limited survey will preferentially find objects with smaller viewing angles α within the corresponding groups of $\alpha < \theta$ and $\alpha > \theta$, as is clear from Fig. 9. However, this may be regarded as a next-order correction to the bias considered here and does not significantly affect our results, as we verify in §5.

As was said before, the $N_{\text{H,eq}}$ values for our obscured objects are estimated from their measured N_{H} columns as $N_{\text{H,eq}} = 1.27N_{\text{H}}$. However, we cannot determine similarly

the torus column densities for our unobscured AGN¹. Therefore, we simply assume that $N_{\text{H,eq}} = 10^{24} \text{ cm}^{-2}$ for these objects, since this is approximately the median value of the inferred intrinsic absorption column distribution for obscured AGN (see Fig. 11).

(ii) Second, we calculate for each source the volume of the Universe, $V_{\text{max},i}(L_{\text{obs},i})$, over which AGN with such observed luminosity can be detected in the *INTEGRAL* survey. Since the detection limit for a given hard X-ray instrument (IBIS in our case) is actually determined by photon counts, it should depend on the observed X-ray spectral shape, which for the problem at hand is affected by absorption and reflection in the torus (see examples of AGN spectra in Fig. 8). We correct $V_{\text{max},i}$ for this effect, but this correction proves to be negligible (as is the k -correction due to cosmological redshift). As a result, we obtain essentially the same $V_{\text{max},i}$ for our sources as we used in constructing the observed LF in §3).

(iii) The final step consists of summing up the $1/V_{\text{max},i}$ contributions of the individual sources, i.e. adding the $1/V_{\text{max},i}$ for each AGN of a given class (unobscured or obscured) to the space density of such objects within a luminosity bin containing $L_{\text{intr},i}$ (rather than $L_{\text{obs},i}$) for this source.

To obtain analytic forms of the intrinsic LFs, we use the same broken power-law model as for our observed LFs but a different likelihood estimator:

$$\mathcal{L} = -2 \sum_i \ln \frac{\phi(L_{\text{intr},i}) \int V_{\text{max}}(L_{\text{intr},i}, N_{\text{H,eq}}) d \log N_{\text{H,eq}}}{\int \int \phi(L_{\text{intr}}) V_{\text{max}}(L_{\text{intr}}, N_{\text{H,eq}}) d \log L_{\text{intr}} d \log N_{\text{H,eq}}} \quad (7)$$

Here $L_{\text{intr},i}$ are the same estimates of the intrinsic luminosities of our objects as we used before to construct the binned intrinsic LFs (i.e. calculated from $L_{\text{obs},i}$ using the actual $N_{\text{H},i}$ estimates for the obscured AGN and assuming that $N_{\text{H,eq}} = 10^{24} \text{ cm}^{-2}$ for the unobscured ones), but $V_{\text{max}}(L_{\text{intr}}, N_{\text{H,eq}})$ is now the volume over which AGN with given intrinsic luminosity L_{intr} and torus column density $N_{\text{H,eq}}$ can be detected in the *INTEGRAL* survey. To calculate these volumes, we again use the α -averaged quantities $R_{\text{unobsc}}(\theta, N_{\text{H,eq}})$ (in fitting the intrinsic LF of unobscured AGN) and $R_{\text{obsc}}(\theta, N_{\text{H,eq}})$ (in fitting the intrinsic LF of obscured AGN). The integrals over $d \log N_{\text{H,eq}}$ in equation (7) are computed from 10^{22} to 10^{26} cm^{-2} , i.e. we assume that the intrinsic distribution of torus column densities is log-uniform over this range, as suggested by the result of our preceding analysis shown in Fig. 11.

Figure 12 shows the resulting intrinsic LFs for unobscured and obscured AGN, calculated assuming $\theta = 30^\circ$ for Model A and Model B. We see that in the former case, the shapes of the intrinsic LFs of unobscured and obscured AGN are clearly different from each other, although to a lesser degree that it was for the observed LFs (Fig. 6) from which they derive. However, for Model B the intrinsic LFs of unobscured and obscured AGN are not significantly different in shape from each other. These conclusions are verified by

¹ In principle, one could try to estimate $N_{\text{H,eq}}$ for unobscured AGN from the contribution of the reflection component to the observed spectrum, but that requires high-quality hard X-ray data, which is not always available, and is model-dependent. In particular, the result will depend on the unknown opening angle θ .

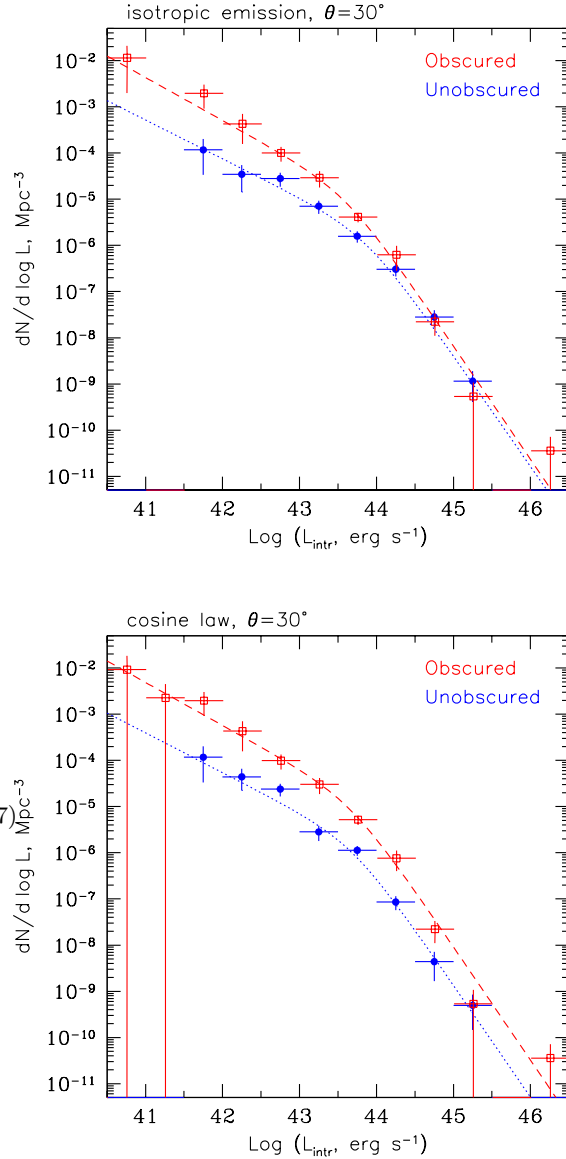


Figure 12. *Top:* Reconstructed intrinsic hard X-ray LFs of unobscured (blue filled circles) and obscured (red empty squares) AGN, fitted by a broken power law (the best-fit parameters are given in Table 2) (blue dotted line and red dashed line, respectively). Model A is adopted, with $\theta = 30^\circ$. *Bottom:* The same, but for Model B.

the best-fit parameters obtained for these LFs (see Table 2). Note that the derived intrinsic LFs (both binned and analytic ones) are only weakly sensitive to the torus half-opening angle θ that was assumed in constructing them, and nearly the same results are obtained for $\theta = 30^\circ$ and $\theta = 45^\circ$. This is due to the weak sensitivity of the R_{unobsc} and R_{obsc} factors to θ (see Fig. 10).

The transformation of the observed binned LFs to the intrinsic ones can be understood as follows: (i) all unobscured AGN making up the LF shift by the same amount, $\log L_{\text{obs}}/L_{\text{intr}} \sim 0.1$ and ~ 0.3 for Model A and Model B, respectively, to the left along the luminosity axis (since we have assumed the same equatorial optical depth of the

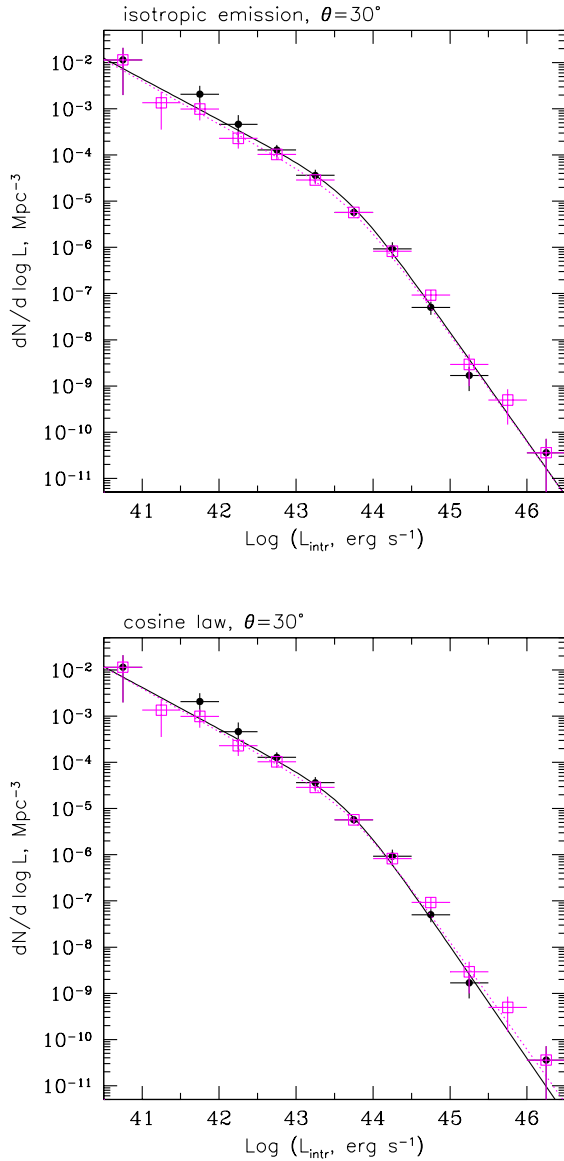


Figure 13. *Top:* Reconstructed intrinsic hard X-ray LF of local AGN (black filled circles), fitted by a broken power law (black solid line, the best-fit parameters are given in Table 2). Model A is adopted, with $\theta = 30^\circ$. For comparison, the observed LF is also shown (magenta empty squares and dotted line). *Bottom:* The same, but for Model B.

torus, $N_{\text{H,eq}} = 10^{24} \text{ cm}^{-2}$, for all of our unobscured objects), and (ii) each obscured AGN from the *INTEGRAL* sample moves its own distance to the right-hand side of the plot, this shift being small for lightly obscured objects ($N_{\text{H}} < 10^{24} \text{ cm}^{-2}$) but substantial (up to $\log L_{\text{intr}}/L_{\text{obs}} \sim 1$ for $N_{\text{H}} \gtrsim 10^{25} \text{ cm}^{-2}$) for heavily obscured ones.

Finally, we can calculate the intrinsic LF of the entire local AGN population, by summing up the contributions of unobscured and obscured sources. In obtaining the analytic fit in this case, we define $V_{\text{max}}(L_{\text{intr}}, N_{\text{H,eq}})$ as follows:

$$V_{\text{max}} = V_{\text{max,unobsc}}(1 - \cos \theta) + V_{\text{max,obsc}} \cos \theta, \quad (8)$$

where $V_{\text{max,unobsc}}(L_{\text{intr}}, N_{\text{H,eq}})$ and $V_{\text{max,obsc}}(L_{\text{intr}}, N_{\text{H,eq}})$

are the corresponding volumes for unobscured and obscured AGN. The resulting LF is shown in Fig. 13 and its best-fit parameters are presented in Table 2.

One can see that the total intrinsic LF is not very different from the total observed LF. This means that the two effects observed in Fig. 12, namely the shift of the LF of unobscured AGN to lower luminosities and the shift of the LF of obscured AGN to higher luminosities almost compensate each other, with this conclusion being only weakly sensitive to the assumed torus opening angle and angular dependence of intrinsic emission.

4.5 Total AGN space density

Integration of the total intrinsic and observed LFs over luminosity suggests that the cumulative hard X-ray luminosity density of local AGN may be underestimated by the observed LF by $\sim 10\text{--}30\%$, although this increase is statistically insignificant (see Table 2). Specifically, the intrinsic luminosity density of AGN with $L_{\text{intr}} > 10^{40.5} \text{ erg s}^{-1}$ is found to be $\sim 1.8 \times 10^{39} \text{ erg s}^{-1} \text{ Mpc}^{-3}$ (17–60 keV), with the exact value slightly depending on our assumptions (see Table 2).

For our assumed intrinsic AGN spectrum ($dN/dE \propto E^{-1.8} e^{-E/200 \text{ keV}}$), the ratio of luminosities in the 2–10 keV and 17–60 keV energy bands is about unity. Therefore, the luminosity density of AGN with $L_{\text{intr}} > 10^{40.5} \text{ erg s}^{-1}$ may be estimated at $\sim 1.8 \times 10^{39} \text{ erg s}^{-1} \text{ Mpc}^{-3}$ also in the standard X-ray band (2–10 keV). We may compare this value with a prediction for $z = 0$ based on a redshift-dependent intrinsic luminosity function derived by Ueda et al. (2014) using a large heterogeneous sample of AGN compiled from various surveys. Integration of this LF over the luminosity range from $10^{40.5}$ to $10^{46.5} \text{ erg s}^{-1}$ gives $\sim 8 \times 10^{38} \text{ erg s}^{-1} \text{ Mpc}^{-3}$ (2–10 keV), which is a factor of ~ 2 smaller than the above estimate. In reality, the $L_{\text{intr}}(17\text{--}60 \text{ keV})/L_{\text{intr}}(2\text{--}10 \text{ keV})$ ratio may well be ~ 1.5 rather than ~ 1 due to the expected presence in AGN spectra of a Compton reflection component associated with the accretion disk. In fact, this component was already discussed in §4.1 as one of the reasons why hard X-ray emission may be intrinsically collimated in AGN and is implicitly taken into account in our anisotropic Model B. Taking this spectral component into account, we can lower our estimate of the luminosity density to $\sim 1.2 \times 10^{39} \text{ erg s}^{-1} \text{ Mpc}^{-3}$ (2–10 keV), which is still higher than the Ueda et al. (2014) result by a factor of ~ 1.5 . The remaining difference may be related to the different procedures used in these works to construct the intrinsic LFs and to the larger and more complete sample of local heavily obscured AGN used in our study.

4.6 Intrinsic dependence of obscured AGN fraction on luminosity

Similarly to the observed LF, the observed dependence of the fraction of obscured AGN on luminosity (Fig. 4) must be affected by AGN detection biases. By removing these biases one can obtain an intrinsic dependence of the obscured AGN fraction on luminosity. To this end, we should simply divide the intrinsic LF of obscured AGN by the total intrinsic LF. The result is presented in Fig. 14 for $\theta = 30^\circ$, Model A and Model B, and in Fig. 15 for $\theta = 45^\circ$.

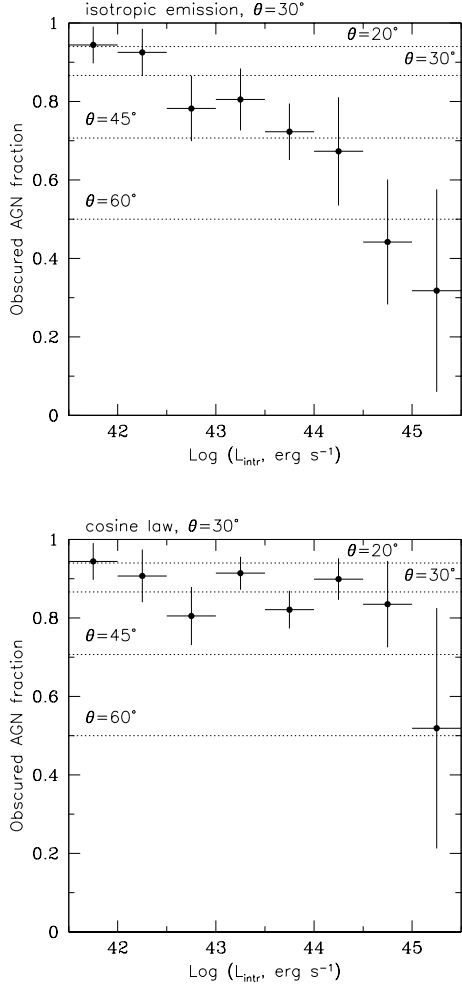


Figure 14. *Top:* Reconstructed intrinsic fraction of obscured AGN as a function of intrinsic hard X-ray luminosity, calculated for $\theta = 30^\circ$ and Model A. *Bottom:* The same but for Model B. The dotted lines indicate the fraction of the sky that will be screened from the central source by a torus with half-opening angle $\theta = 20^\circ, 30^\circ, 45^\circ$ or 60° .

We see that in the case of isotropic emission the declining trend of obscured AGN fraction with luminosity is retained upon removing the absorption bias, although the intrinsic obscured fraction at any luminosity is significantly higher compared to the observed fraction (see Fig. 4). We can interpret this result in terms of the torus opening angle, i.e. the fraction of the sky that will be shielded from the central source by a toroidal structure of gas. To this end, we have drawn in Figs. 14 and 15 four horizontal lines corresponding to $\theta = 20^\circ, 30^\circ, 45^\circ$ and 60° . We see that if the central sources in AGN are isotropic, then the torus opening angle must be smaller than 30° in low-luminosity objects ($L_{\text{intr}} \lesssim 10^{42.5} \text{ erg s}^{-1}$) and increasing to $\sim 45^\circ$ – 60° in high-luminosity ones ($L_{\text{intr}} \gtrsim 10^{44} \text{ erg s}^{-1}$).

If, however, the emission from the central SMBH is collimated as $dL_{\text{intr}}/d\Omega \propto \cos \alpha$, then the derived intrinsic dependence of the obscured AGN fraction on luminosity is in fact consistent with the opening angle of the torus being

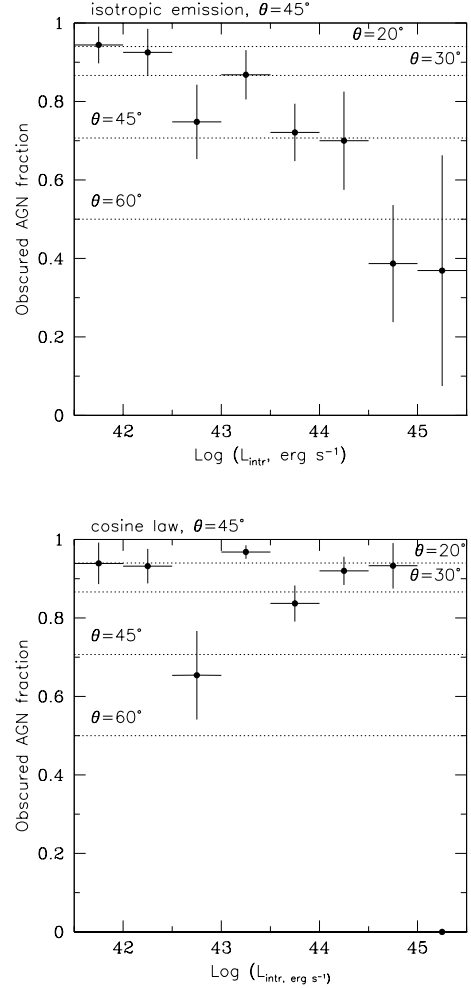


Figure 15. The same as Fig. 14, but for $\theta = 45^\circ$.

constant with luminosity, namely $\theta \sim 30^\circ$ – see the bottom panel in Fig. 14.

Importantly, these conclusions are almost insensitive to the opening angle (within the range $\theta \sim 20$ – 60°) of the torus that we actually assumed in deriving the intrinsic luminosity dependences of the obscured AGN fraction (compare the results for $\theta = 45^\circ$ and $\theta = 30^\circ$ in Figs. 14 and 15). This is again due to the fact that the R_{unobsc} and R_{obsc} ratios, which characterise observational biases for our AGN sample and which we have corrected for, are, for a given emission law (Model A or Model B), primarily determined by the torus column density (see Fig. 10). Hence, the derived intrinsic luminosity dependences of the obscured AGN fraction are quite robust but depend on the actual degree of collimation of the AGN central source.

5 DIRECT CONVOLUTION MODEL

We have demonstrated that positive bias with respect to unobscured AGN and negative bias with respect to obscured AGN in flux-limited hard X-ray surveys together strongly affect the observed dependence of the obscured AGN fraction

on luminosity. Our preceding analysis consisted of converting the observed LFs of unobscured and obscured AGN to the intrinsic LFs of these populations. In solving this 'inverse problem', we used a number of simplifications that we noted were unlikely to have significant impact on our results. In particular, we used the viewing angle-averaged conversion factors $R_{\text{unobsc}}(L_{\text{intr}}, N_{\text{H,eq}})$ and $R_{\text{obsc}}(L_{\text{intr}}, N_{\text{H,eq}})$ rather than the $R_{\text{unobsc}}(L_{\text{intr}}, N_{\text{H,eq}}, \alpha)$ and $R_{\text{obsc}}(L_{\text{intr}}, N_{\text{H,eq}}, \alpha)$ ratios from which they derive. We also assumed a fixed torus column density, $N_{\text{H,eq}} = 10^{24} \text{ cm}^{-2}$, for all of our unobscured AGN. To verify that these assumptions were reasonable, we now perform a 'direct convolution' test, as described below:

(i) Assume that the tori in local AGN have the same half-opening angle θ .

(ii) Assume that local AGN are oriented randomly with respect to us.

(iii) Assume that the AGN central source is isotropic or, alternatively, emitting according to Lambert's law ($dL_{\text{intr}}/d\Omega \propto \cos \alpha$).

(iv) Assume that the intrinsic distribution of AGN torus column densities $N_{\text{H,eq}}$ does not depend on luminosity and is log-uniform between $N_{\text{H,min}}$ and $N_{\text{H,max}}$. Such a distribution, with $N_{\text{H,min}} \sim 10^{22} \text{ cm}^{-2}$ and $N_{\text{H,max}} \sim 10^{26} \text{ cm}^{-2}$, approximately matches the real $N_{\text{H,eq}}$ distribution we have inferred using the *INTEGRAL* sample (see Fig. 11).

(v) Adopt the intrinsic AGN LF as derived in our preceding analysis for given θ and emission law (see Table 2).

(vi) Use the above set of assumptions specifying the intrinsic properties of the local AGN population to simulate, using our torus obscuration model, AGN properties as would be observed in the *INTEGRAL* survey.

The main difference with respect to the inverse problem is that the $L_{\text{obs}}/L_{\text{intr}}$ ratio now explicitly depends on the viewing angle, which is randomly drawn for each simulated source, and on $N_{\text{H,eq}}$, which is drawn from the assumed log-uniform distribution for each simulated source, both for obscured AGN and for unobscured ones.

Figure 16 shows the simulated luminosity dependences of the observed obscured AGN fraction for $\theta = 30^\circ$ and either isotropic or cosine-law emission; Fig. 17 shows the corresponding results for $\theta = 45^\circ$. As our baseline $N_{\text{H,eq}}$ distribution we use $N_{\text{H,min}} = 10^{22} \text{ cm}^{-2}$ and $N_{\text{H,max}} = 10^{26} \text{ cm}^{-2}$ (solid lines), but we also show results obtained for $N_{\text{H,min}} = 10^{22} \text{ cm}^{-2}$ and $N_{\text{H,max}} = 10^{25} \text{ cm}^{-2}$ and for $N_{\text{H,min}} = 10^{23} \text{ cm}^{-2}$ and $N_{\text{H,max}} = 10^{26} \text{ cm}^{-2}$. The results of simulations are compared with the luminosity dependence actually observed with *INTEGRAL*.

We see that the luminosity dependence of the observed obscured AGN fraction predicted for the case of isotropic emission and $\theta = 30^\circ$ is inconsistent with the *INTEGRAL* data ($\chi^2 = 32.6$ per 8 data points between $L_{\text{obs}} = 10^{41.5}$ and $10^{45.5} \text{ erg s}^{-1}$). The isotropic model with a larger torus opening angle, $\theta = 45^\circ$, provides a better match but the fit is nevertheless poor ($\chi^2 = 15.2$ per 8 data points). Among the four presented cases, the best agreement between simulations and observations is achieved in the case of cosine-law emission and $\theta = 30^\circ$ ($\chi^2 = 9.0$ per 8 data points). These results confirm our previously reached conclusion that unless hard X-ray emission in AGN is intrinsically collimated,

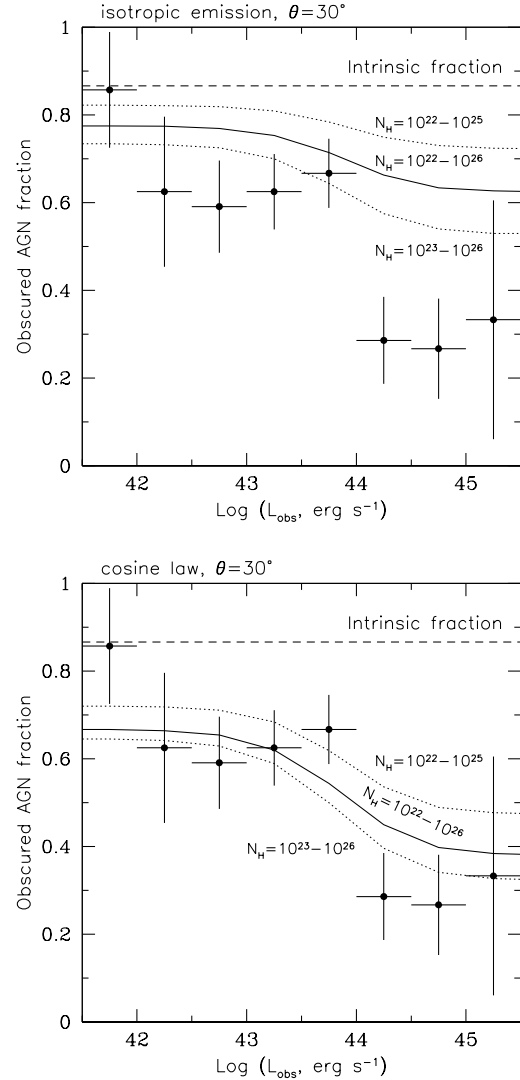


Figure 16. Simulated dependence of the observed fraction of obscured AGN on observed hard X-ray luminosity for $\theta = 30^\circ$ and either isotropic (*top*) or cosine-law (*bottom*) emission, for various ranges of $N_{\text{H,eq}}$ (solid and dotted lines). The intrinsic obscured fraction is indicated by the dashed line. For comparison, the corresponding dependence observed with *INTEGRAL* is reproduced from Fig. 4 (data points with error bars).

there must be an intrinsic declining trend of the torus opening angle with increasing AGN luminosity.

Nevertheless, Figs. 16 and 17 clearly demonstrate that biases associated with detection of AGN in flux-limited hard X-ray surveys *inevitably lead to the observed fraction of obscured AGN being dependent on luminosity even if this quantity has no intrinsic luminosity dependence*. Specifically, in such a case, the observed obscured fraction approaches a constant value in the limit of $L \ll L_*$, and another, lower limiting value at $L \gg L_*$. It is easy to show that, if the intrinsic ratio of obscured and unobscured AGN is $(N_{\text{obsc}}/N_{\text{unobsc}})_{\text{intr}}$, then their observed ratio will be:

$$\left(\frac{N_{\text{obsc}}}{N_{\text{unobsc}}}\right)_{\text{obs}} = \left(\frac{N_{\text{obsc}}}{N_{\text{unobsc}}}\right)_{\text{intr}} \left(\frac{\langle R_{\text{obsc}} \rangle}{\langle R_{\text{unobsc}} \rangle}\right)^\gamma, \quad (9)$$

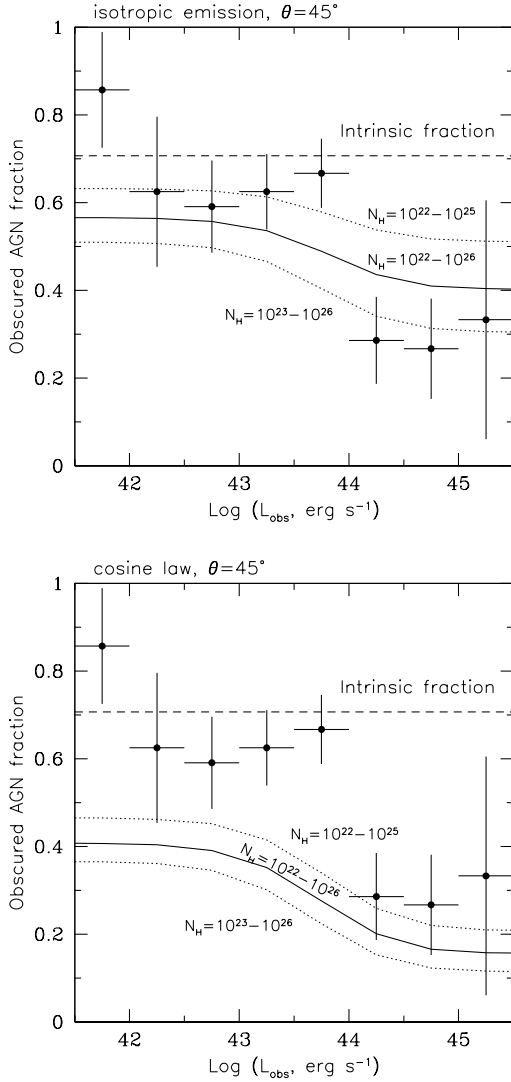


Figure 17. The same as Fig. 16, but for $\theta = 45^\circ$.

where $\langle R_{\text{obsc}} \rangle$ and $\langle R_{\text{unobsc}} \rangle$ are the appropriately ensemble-averaged bias factors ($= L_{\text{obs}}/L_{\text{intr}}$) for unobscured and obscured AGN, respectively, and γ is the (effective) slope of the luminosity function. For example, in the case of cosine-law emission and $\theta = 30^\circ$, the corresponding bias factors averaged over the log-uniform $N_{\text{H,eq}}$ distribution (see Fig. 10) are $\langle R_{\text{unobsc}} \rangle \sim 2$ and $\langle R_{\text{obsc}} \rangle \sim 0.7$, whereas $(N_{\text{obsc}}/N_{\text{unobsc}})_{\text{intr}} = 6.46$. Therefore, for our inferred intrinsic AGN LF, with $\gamma \sim 0.9$ and $\gamma \sim 2.4$ in the low- and high-luminosity ends, respectively, and $L_* \sim 10^{43.7}$, we may expect $(N_{\text{obsc}}/N_{\text{unobsc}})_{\text{obs}} \sim 2.5$ and $(N_{\text{obsc}}/N_{\text{unobsc}})_{\text{obs}} \sim 0.5$ at $L \ll 10^{43.7}$ and $L \gg 10^{43.7}$ erg s $^{-1}$, respectively. This corresponds to the obscured AGN fractions $N_{\text{obsc}}/(N_{\text{unobsc}} + N_{\text{obsc}}) \sim 0.71$ and ~ 0.33 , respectively, which is approximately what we see in Fig. 16 for the results of simulations with the cosine-law emission law and $\theta = 30^\circ$.

Figure 18 shows how our direct convolution model predicts the observed LFs of unobscured and obscured AGN in the case of cosine-law emission and $\theta = 30^\circ$. We see that for unobscured AGN, the simulated observed LF fits the *INTE-*

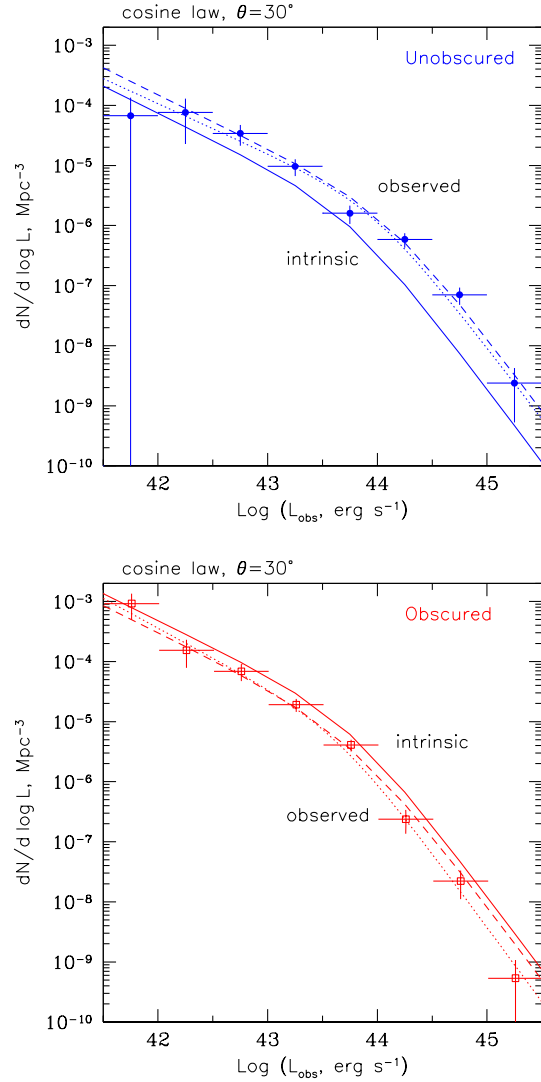


Figure 18. *Top:* Simulated observed LF of unobscured AGN (dashed line) for $\theta = 30^\circ$, cosine-law emission, $N_{\text{H,min}} = 10^{22}$ cm $^{-2}$ and $N_{\text{H,max}} = 10^{26}$ cm $^{-2}$, in comparison with the LF of unobscured AGN observed by *INTEGRAL* (data points with error bars and their fit by a broken power-law model – dotted line). The solid line shows the assumed intrinsic LF of unobscured AGN (equal to the total AGN LF multiplied by $(1 - \cos \theta)$), which was previously (in §4.4) derived from the *INTEGRAL* data using an inverse approach. *Bottom:* The same, but for obscured AGN. In this case the intrinsic LF of obscured AGN is equal to the total intrinsic LF multiplied by $\cos \theta$.

GRAL data well. In the case of obscured AGN, the match between the simulated and actually observed LFs is good below $L_{\text{obs}} \sim 10^{44}$ erg s $^{-1}$, but a significant deviation is evident at higher luminosities. This probably reflects the intrinsic differences between the inverse and direct approaches to the considered problem, discussed at the beginning of this section. Nevertheless, this difference does not significantly affect the conclusions of this study.

Note that in reality the situation may be more complicated. For example, the intrinsic $N_{\text{H,eq}}$ distribution may depend on luminosity. Also, the obscuring gas may be clumpy,

so that the N_{H} distribution observed for obscured AGN may represent not only the distribution of torus column densities over the AGN population but also the distribution of line-of-sight columns over different observing directions for a given AGN torus. It would be interesting to study this and other possibilities in future work, when significantly larger samples of hard X-ray selected AGN become available.

6 DISCUSSION AND SUMMARY

We utilised a sample of about 150 local ($z \lesssim 0.2$) hard X-ray selected AGN, with reliable information on X-ray absorption columns, to find out how strongly the observed declining trend of the obscured AGN fraction with increasing luminosity may be affected by selection effects. Using a torus-obscuration model and a state-of-the-art radiative transfer code, we demonstrated that there must exist not only a negative bias, due to absorption in the torus, in finding obscured AGN in hard X-ray flux limited surveys, but also a positive bias in detecting unobscured AGN – due to reflection by the torus of part of the radiation emitted by the central source towards the observer. We further pointed out that these two biases may in fact be even stronger if one takes into account plausible intrinsic collimation of hard X-ray emission along the axis of the obscuring torus, which can arise both in the hot corona where the hard X-ray emission presumably originates and as a result of reflection of part of this radiation by the underlying, optically thick accretion disk.

We demonstrated that for an AGN luminosity function that steepens at high luminosities, which is indeed the case, these observational biases should inevitably lead to the observed fraction of obscured AGN being smaller in the high-luminosity end of the LF than in the low-luminosity end even if the obscured AGN fraction has no intrinsic luminosity dependence. Moreover, even in the low-luminosity part of the LF, the observed obscured fraction will be lower than its intrinsic value.

We explored two possibilities for the central hard X-ray source in AGN: (i) isotropic emission and (ii) emission collimated according to Lambert’s law, $dL/d\Omega \propto \cos \alpha$. In the former case, the intrinsic (i.e. corrected for the biases discussed above) obscured AGN fraction reconstructed from our *INTEGRAL* sample still shows a declining trend with luminosity, although the inferred intrinsic obscured fraction is larger than the observed one at any luminosity. Namely, the obscured fraction is larger than $\sim 85\%$ at $L \lesssim 10^{42.5} \text{ erg s}^{-1}$ (17–60 keV), and decreases to $\lesssim 60\%$ at $L \gtrsim 10^{44} \text{ erg s}^{-1}$. In terms of the half-opening angle θ of an obscuring torus, this implies that $\theta \lesssim 30^\circ$ in lower-luminosity AGN, and $\theta \gtrsim 45^\circ$ in higher-luminosity ones. If, however, the emission from the central SMBH is collimated as $dL/d\Omega \propto \cos \alpha$, then the derived intrinsic dependence of the obscured AGN fraction is consistent with the opening angle of the torus being constant with luminosity, namely $\theta \sim 30^\circ$.

At the moment, we regard both possibilities – intrinsic obscuring AGN fraction declining with luminosity or being constant – as feasible, as they depend on the presently poorly understood angular emission diagram of the central source in AGN. We note however that a luminosity-independent obscured AGN fraction might be consistent with findings of some studies based on non-X-ray selected

AGN samples (see Lawrence & Elvis 2010 for a discussion). We also note that the intrinsic ratio of obscured to unobscured AGN that follows from our study, which changes with luminosity from $\gtrsim 6 : 1$ to $\sim 1 : 1$ in the case of isotropic emission and is $\sim 6 : 1$ in the case of cosine-law emission, is not very different from the $\sim 4 : 1$ ratio inferred for optically selected AGN by Maiolino & Rieke (1995). A more careful comparison of these and other existing estimates of the ratio of obscured and unobscured AGN in future work may help us get insight into the geometrical and physical properties of obscuration in AGN, which may be different in X-ray, optical, infrared and radio bands.

The intrinsic dependence of the obscured AGN fraction on luminosity derived here can find application in modelling the cosmic X-ray background (CXB). Importantly, the inferred obscured fractions are somewhat larger (even without allowance for possible intrinsic collimation of X-ray emission in AGN) than those adopted in some popular CXB synthesis models (e.g. Treister & Urry 2005; Gilli, Comastri, & Hasinger 2007; Ueda et al. 2014) – for example compare our Figs. 14 and 15 with Fig. 13 in Gilli, Comastri, & Hasinger 2007 and Fig. 5 in Ueda et al. 2014 (note, however, that these plots use the 2–10 keV energy band while we use 17–60 keV).

As a byproduct, we reconstructed the intrinsic hard X-ray luminosity function of local AGN and estimated the total number density and luminosity density of AGN with $L > 10^{40.5} \text{ erg s}^{-1}$ (17–60 keV and 2–10 keV), which may be used as reference $z = 0$ values in the study of cosmic AGN evolution and in modelling the cosmic X-ray background.

The constraints on the intrinsic dependence of the obscured AGN fraction on luminosity obtained in this work can be improved in the near future using larger samples of hard X-ray selected AGN from *INTEGRAL*, *Swift* and *NuSTAR* surveys (see Lansbury et al. 2015 for a new constraint on the abundance of heavily obscured AGN from *NuSTAR* data). Note however that it will be practically impossible to improve the current, fairly uncertain estimate of the obscured AGN fraction at the highest luminosities ($\gtrsim 10^{45} \text{ erg s}^{-1}$) in the local Universe, since the *INTEGRAL* and *Swift* all-sky surveys are sensitive enough to detect all such objects in the local ($z \lesssim 0.2$) Universe and have found just a few of them because of the very low space density thereof.

We finally note that AGN selection effects similar to those discussed for hard X-ray surveys in this work should also affect obscured AGN fractions inferred from samples selected in X-rays (at energies below 10 keV). This should be studied in future work.

ACKNOWLEDGMENTS

This study was supported by the Russian Foundation for Basic Research (grant 13-02-01365). We thank the referee for useful comments.

APPENDIX A: AGN CATALOGUE

Table A1 presents the sample of non-blazar AGN at $|b| > 5^\circ$ used in this work. It is based on the catalogue of sources (Krivonos et al. 2010b) detected dur-

ing the *INTEGRAL*/IBIS 7-year all-sky survey. After publication of this catalogue, three previously unidentified sources, IGR J13466+1921, IGR J14488–4009 and IGR J17036+3734 have been proved to be AGN and hence added to our sample. For 31 nearby (closer than 40 Mpc) objects we adopt distance estimates from the Extragalactic Distance Database (EDD)², whereas the distances of the remaining objects are estimated from their redshifts, which are adopted from NED. The quoted hard X-ray luminosities are observed ones, calculated from the adopted distances and measured hard X-ray (17–60 keV) fluxes (Krivonos et al. 2010b).

For this study, the most important AGN property is X-ray absorption column density. The corresponding information has been updated with respect to our previous publications (Sazonov & Revnivtsev 2004; Sazonov et al. 2007, 2012) whenever necessary and possible. The last column of Table A1 provides relevant references.

REFERENCES

- Agostinelli S., et al., 2003, *NIMPA*, 506, 250
Aird J., Coil A. L., Georgakakis A., Nandra K., Barro G., Pérez-González P. G., 2015, *MNRAS*, 451, 1892
Ajello M., Alexander D. M., Greiner J., Madejski G. M., Gehrels N., Burlon D., 2012, *ApJ*, 749, 21
Bauer F. E., et al., 2014, arXiv, arXiv:1411.0670
Beckmann V., et al., 2009, *A&A*, 505, 417
Braitto V., Ballo L., Reeves J. N., Risaliti G., Ptak A., Turner T. J., 2013, *MNRAS*, 428, 2516
Brightman M., Nandra K., 2011, *MNRAS*, 413, 1206
Brightman M., et al., 2015, *ApJ*, 805, 41
Buchner J., et al., 2015, *ApJ*, 802, 89
Burlon D., Ajello M., Greiner J., Comastri A., Merloni A., Gehrels N., 2011, *ApJ*, 728, 58
Cappi M., et al., 2006, *A&A*, 446, 459
Churazov E., Sazonov S., Sunyaev R., Revnivtsev M., 2008, *MNRAS*, 385, 719
Comastri A., Iwasawa K., Gilli R., Vignali C., Ranalli P., Matt G., Fiore F., 2010, *ApJ*, 717, 787
Cullen D. E., Perkins S. T., Rathkopf J. A., 1990, The 1989 Livermore Evaluated Photon Data Library (EPDL), UCRL-ID-103424, Lawrence Livermore National Laboratory
de Rosa A., et al., 2012, *MNRAS*, 420, 2087
Dewangan G. C., Griffiths R. E., 2005, *ApJ*, 625, L31
Eguchi S., Ueda Y., Awaki H., Aird J., Terashima Y., Mushotzky R., 2011, *ApJ*, 729, 31
Fukazawa Y., et al., 2011, *ApJ*, 727, 19
Gallo L. C., Lehmann I., Pietsch W., Boller T., Brinkmann W., Friedrich P., Grupe D., 2006, *MNRAS*, 365, 688
Gilli R., Comastri A., Hasinger G., 2007, *A&A*, 463, 79
Greenhill L. J., Tilak A., Madejski G., 2008, *ApJ*, 686, L13
Guainazzi M., Fabian A. C., Iwasawa K., Matt G., Fiore F., 2005a, *MNRAS*, 356, 295
Guainazzi M., Matt G., Perola G. C., 2005b, *A&A*, 444, 119
Hasinger G., 2004, *NuPhS*, 132, 86
Hasinger G., 2008, *A&A*, 490, 905
Ikeda S., Awaki H., Terashima Y., 2009, *ApJ*, 692, 608
Immler S., Brandt W. N., Vignali C., Bauer F. E., Crenshaw D. M., Feldmeier J. J., Kraemer S. B., 2003, *AJ*, 126, 153
Kaastra J. S., Mewe R., 1993, *A&AS*, 97, 443
Kippen R. M., 2004, *NewAR*, 48, 221
Krivonos R., Revnivtsev M., Tsygankov S., Sazonov S., Vikhlinin A., Pavlinsky M., Churazov E., Sunyaev R., 2010, *A&A*, 519, A107
Krivonos R., Tsygankov S., Revnivtsev M., Grebenev S., Churazov E., Sunyaev R., 2010, *A&A*, 523, AA61
Krivonos R., Sazonov S., Churazov E., 2015, in preparation
Krongold Y., et al., 2009, *ApJ*, 690, 773
La Franca F., et al., 2005, *ApJ*, 635, 864
Landi R., et al., 2007, *ATel*, 1274, 1
Landi R., et al., 2009, *A&A*, 493, 893
Landi R., Bassani L., Malizia A., Stephen J. B., Bazzano A., Fiacchi M., Bird A. J., 2010, *MNRAS*, 403, 945
Lansbury G. B., et al., 2015, *ApJ*, 809, 115
Lawrence A., Elvis M., 1982, *ApJ*, 256, 410
Lawrence A., Elvis M., 2010, *ApJ*, 714, 561
Levenson N. A., Cid Fernandes R., Jr., Weaver K. A., Heckman T. M., Storchi-Bergmann T., 2001, *ApJ*, 557, 54
Lewis K. T., Eracleous M., Gliozzi M., Sambruna R. M., Mushotzky R. F., 2005, *ApJ*, 622, 816
Maiolino R., Rieke G. H., 1995, *ApJ*, 454, 95
Maiolino R., Salvati M., Bassani L., Dadina M., della Ceca R., Matt G., Risaliti G., Zamorani G., 1998, *A&A*, 338, 781
Magdziarz P., Zdziarski A. A., 1995, *MNRAS*, 273, 837
Malizia A., et al., 2007, *ApJ*, 668, 81
Malizia A., et al., 2008, *MNRAS*, 389, 1360
Malizia A., Stephen J. B., Bassani L., Bird A. J., Panessa F., Ubertini P., 2009, *MNRAS*, 399, 944
Malizia A., Bassani L., Bazzano A., Bird A. J., Masetti N., Panessa F., Stephen J. B., Ubertini P., 2012, *MNRAS*, 426, 1750
Matt G., Bianchi S., Marinucci A., Guainazzi M., Iwawasa K., Jimenez Bailon E., 2013, *A&A*, 556, A91
Mayo J. H., Lawrence A., 2013, *MNRAS*, 434, 1593
Molina M., et al., 2008, *MNRAS*, 390, 1217
Molina M., et al., 2009, *MNRAS*, 399, 1293
Molina M., Landi R., Bassani L., Malizia A., Stephen J. B., Bazzano A., Bird A. J., Gehrels N., 2012, *A&A*, 548, A32
Moran E. C., Eracleous M., Leighly K. M., Chartas G., Filippenko A. V., Ho L. C., Blanco P. R., 2005, *AJ*, 129, 2108
Murphy K. D., Yaqoob T., 2009, *MNRAS*, 397, 1549
Noguchi K., Terashima Y., Awaki H., 2009, *ApJ*, 705, 454
Panessa F., et al., 2008, *A&A*, 483, 151
Panessa F., et al., 2011, *MNRAS*, 417, 2426
Parisi P., et al., 2009, *A&A*, 507, 1345
Petrucci P. O., et al., 2007, *A&A*, 470, 889
Pozdnyakov L. A., Sobol I. M., Sunyaev R. A., 1983, *AS-PRv*, 2, 189
Puccetti S., et al., 2014, *ApJ*, 793, 26
Reeves J. N., Turner M. J. L., 2000, *MNRAS*, 316, 234
Revnivtsev M., Sazonov S., Churazov E., Trudolyubov S., 2006, *A&A*, 448, L49
Revnivtsev M., Sunyaev R., Lutovinov A., Sazonov S., 2007, *ATel*, 1253, 1

² <http://edd.ifa.hawaii.edu/>

Table A1. *INTEGRAL* 7-year sample of non-blazar AGN at $|b| > 5^\circ$.

Object	z	D Mpc	Ref.	$\log L_{17-60 \text{ keV}}$ erg s $^{-1}$	N_{H} 10^{22} cm^{-2}	Ref.
IGR J00040+7020	0.0960	442.4		44.31	3	2
SWIFT J0025.8+6818	0.0120	52.0		42.51	> 1000	3
MRK 348	0.0150	65.2		43.69	30	4
ESO 297-G018	0.0252	110.4		43.86	50	5
IGR J01528-0326	0.0172	74.9		43.06	14	6
NGC 788	0.0136	59.0		43.33	40	4
MRK 1018	0.0424	188.1		43.69	< 1	7,8
IGR J02086-1742	0.1290	607.6		44.77	< 1	9
LEDA 138501	0.0492	219.4		44.18	< 1	10
MRK 590	0.0264	115.7		43.26	< 1	11
SWIFT J0216.3+5128	0.4220	2322.8		46.15	3	7
MRK 1040	0.0167	72.7		43.40	< 1	12
IGR J02343+3229	0.0162	70.5		43.26	2	13
NGC 985	0.0431	191.3		43.91	< 1	14
NGC 1052	0.0050	19.4	1	41.89	20	15
NGC 1068	0.0038	12.3	1	41.58	> 1000	16
IGR J02524-0829	0.0168	73.1		42.97	12	9
NGC 1142	0.0288	126.5		43.99	50	4
NGC 1194	0.0136	59.0		42.82	$\sim 100?$	17
IGR J03249+4041	0.0476	212.0		43.84	3	18
IGR J03334+3718	0.0550	246.3		44.17	< 1	7,18
NGC 1365	0.0055	18.0	1	42.16	~ 50	19
ESO 548-G081	0.0145	63.0		43.21	< 1	20
3C 105	0.0890	408.2		44.69	30	7,8
3C 111	0.0485	216.1		44.53	< 1	21
IRAS 04210+0400	0.0450	200.0		43.98	30	7,18
3C 120	0.0330	145.4		44.14	< 1	11
UGC 03142	0.0217	94.8		43.59	3	7
CGCG 420-015	0.0294	129.2		43.51	> 1000	3
ESO 033-G002	0.0181	78.9		43.05	1	22
LEDA 075258	0.0160	69.6		42.75	< 1	7,18
XSS J05054-2348	0.0350	154.4		44.13	6	23
IRAS 05078+1626	0.0179	78.0		43.66	< 1	24
ARK 120	0.0327	144.0		44.02	< 1	25
ESO 362-G018	0.0124	53.8		43.10	< 1	26
PIC A	0.0351	154.9		44.01	< 1	11
NGC 2110	0.0078	29.0	1	43.11	14	27
MCG 8-11-11	0.0204	89.0		43.92	< 1	11
MRK 3	0.0135	58.6		43.45	100	28
PMN J0623-6436	0.1289	607.1		44.73	< 1	29
IGR J06239-6052	0.0405	179.4		43.80	20	30
IGR J06415+3251	0.0172	74.9		43.39	16	31
MRK 6	0.0188	81.9		43.52	~ 5	32
IGR J07563-4137	0.0210	91.7		43.08	< 1	33
ESO 209-G012	0.0405	179.4		43.80	< 1	34
IGR J08557+6420	0.0370	163.5		43.64	20	7,18
IRAS 09149-6206	0.0573	257.0		44.19	< 1	10
IGR J09253+6929	0.0390	172.6		43.66	> 100?	35
NGC 2992	0.0077	29.0	1	42.75	1	36
MCG -5-23-16	0.0085	36.8		43.27	2	11
IGR J09522-6231	0.2520	1276.8		45.37	6	37
NGC 3081	0.0080	28.6	1	42.64	100	38
ESO 263-G013	0.0333	146.7		43.72	30	39
NGC 3227	0.0039	26.4	1	42.84	< 1	4
NGC 3281	0.0107	46.3		43.08	200	40
IGR J10386-4947	0.0600	269.6		44.05	1	4
IGR J10404-4625	0.0239	104.6		43.48	3	4
NGC 3516	0.0088	38.0	1	42.87	< 1	11
NGC 3783	0.0097	25.1	1	42.95	< 1	4
IGR J11459-6955	0.2440	1230.9		45.31	< 1	7,41
IGR J12009+0648	0.0360	159.0		43.67	11	31

Table A1. (continued)

Object	z	<i>D</i> Mpc	Ref.	$\log L_{17-60 \text{ keV}}$ erg s ⁻¹	N_{H} 10 ²² cm ⁻²	Ref.
IGR J12026–5349	0.0280	122.9		43.75	2	33
NGC 4051	0.0024	17.1	1	41.97	< 1	11
NGC 4138	0.0030	13.8	1	41.60	8	42
NGC 4151	0.0033	11.2	1	42.66	8	11
IGR J12107+3822	0.0229	100.1		43.14	3	7
NGC 4235	0.0080	31.5	1	42.06	< 1	7
NGC 4253	0.0129	56.0		42.74	< 1	43
NGC 4258	0.0015	7.6	1	40.95	7	44
MRK 50	0.0234	102.4		43.21	< 1	24
NGC 4388	0.0084	16.8	1	42.78	40	36,45
NGC 4395	0.0011	4.7	1	40.55	2	46
NGC 4507	0.0118	51.2		43.56	~ 70	47
ESO 506-G027	0.0250	109.5		43.76	100	48
XSS J12389–1614	0.0367	162.1		43.98	2	33
NGC 4593	0.0090	37.3	1	42.96	< 1	4
WKK 1263	0.0244	106.8		43.39	< 1	31
NGC 4939	0.0104	34.7	1	42.36	> 1000?	49
NGC 4945	0.0019	3.4	1	41.41	400	50
ESO 323-G077	0.0150	65.2		43.06	30	4
IGR J13091+1137	0.0251	109.9		43.64	60	39
IGR J13109–5552	0.1040	481.8		44.71	< 1	7
IGR J13149+4422	0.0366	161.7		43.68	5	13
MCG -03-34-064	0.0165	71.8		43.19	~ 50	36
CEN A	0.0018	3.6	1	41.99	11	27
ESO 383-G018	0.0124	53.8		42.74	20	7,51
MCG -6-30-15	0.0077	25.5	1	42.48	< 1	12
NGC 5252	0.0230	100.6		43.91	5	36
MRK 268	0.0399	176.7		43.81	30	7,18
IGR J13466+1921	0.0850	388.7		44.62	< 1	52
IC 4329A	0.0160	69.6		44.02	< 1	12
LEDA 49418	0.0509	227.2		43.75	2	53
NGC 5506	0.0062	21.7	1	42.92	3	11
IGR J14175–4641	0.0766	348.3		44.21	> 100?	35
NGC 5548	0.0172	74.9		43.27	< 1	11
ESO 511-G030	0.0224	97.9		43.45	< 1	11
NGC 5643	0.0040	11.8	1	41.23	> 1000	3
NGC 5728	0.0094	24.8	1	42.51	200	3
IGR J14488–4009	0.1230	577.1		44.69	6	54
IGR J14552–5133	0.0160	69.6		42.87	< 1	10
IGR J14561–3738	0.0246	107.7		43.20	~ 100	37
IC 4518A	0.0157	68.3		43.07	10	7,18
MRK 841	0.0364	160.8		43.98	< 1	55
NGC 5995	0.0252	110.4		43.66	< 1	11
IGR J15539–6142	0.0149	64.8		42.60	20	10
ESO 389-G002	0.0194	84.6		42.93	6	18
WKK 6092	0.0156	67.8		42.96	< 1	24
IGR J16185–5928	0.0350	154.4		43.55	10	56
ESO 137-G034	0.0092	33.0	1	42.26	> 1000	39
IGR J16385–2057	0.0264	115.7		43.27	< 1	13
IGR J16482–3036	0.0313	137.7		43.85	< 1	4
NGC 6221	0.0050	15.6	1	41.66	1	57
NGC 6240	0.0245	107.3		43.76	250	3
IGR J16558–5203	0.0540	241.6		44.22	< 1	4
IGR J17009+3559	0.1130	526.7		44.74	30	7,18
IGR J17036+3734	0.0650	293.1		44.36	< 1	18
NGC 6300	0.0037	13.1	1	42.02	25	11
IGR J17418–1212	0.0372	164.4		43.86	< 1	4
H 1821+643	0.2970	1541.0		45.58	< 1	11
IC 4709	0.0169	73.6		43.36	12	23
IGR J18249–3243	0.3550	1895.4		45.61	< 1	58
ESO 103-G035	0.0133	57.7		43.43	30	11

Table A1. (continued)

Object	z	D Mpc	Ref.	$\log L_{17-60 \text{ keV}}$ erg s ⁻¹	N_{H} 10 ²² cm ⁻²	Ref.
3C 390.3	0.0561	251.4		44.59	< 1	4
ESO 140-G043	0.0142	61.7		43.14	2	59
ESO 025-G002	0.0289	126.9		43.50	< 1	7,18
IGR J18559+1535	0.0838	382.9		44.54	< 1	4
EXSS 1849.4-7831	0.0420	186.3		44.02	< 1	18
IGR J19077-3925	0.0760	345.4		44.21	< 1	7,18
IGR J19194-2956	0.1668	804.6		45.03	< 1	7,18
ESO 141-G055	0.0371	164.0		44.06	< 1	11
SWIFT J1930.5+3414	0.0633	285.1		44.10	30	6
1H 1934-063	0.0106	45.9		42.56	< 1	60
IGR J19405-3016	0.0520	232.3		43.98	< 1	61
NGC 6814	0.0052	22.0	1	42.42	< 1	12
XSS J19459+4508	0.0539	241.1		44.03	11	33
CYG A	0.0561	251.4		44.67	20	62
ESO 399-IG020	0.0250	109.5		43.25	< 1	7,56
IGR J20286+2544	0.0142	61.7		43.21	50	2,4
4C +74.26	0.1040	481.8		44.99	< 1	11
MRK 509	0.0344	151.7		44.21	< 1	11
RX J2044.0+2833	0.0500	223.1		44.08	< 1	7,18
S5 2116+81	0.0860	393.6		44.72	< 1	63
IGR J21196+3333	0.0510	227.7		43.95	< 1	7,18
NGC 7172	0.0087	31.9	1	42.88	13	11
IGR J22292+6646	0.1120	521.7		44.54	< 1	58
NGC 7314	0.0048	15.9	1	41.92	1	64
MRK 915	0.0241	105.5		43.45	3	7,18
MR 2251-178	0.0640	288.4		44.72	< 1	65
NGC 7465	0.0066	26.5	1	42.32	~ 10	66
NGC 7469	0.0163	70.9		43.44	< 1	4
MRK 926	0.0469	208.8		44.28	< 1	4

References: (1) Distance adopted from the Extragalactic Distance Database, rather than calculated from the redshift; (2) de Rosa et al. (2012); (3) Krivonos et al. (2015); (4) Sazonov et al. (2007); (5) Ueda et al. (2007); (6) Landi et al. (2007); (7) Sazonov et al. (2010); (8) Winter et al. (2009a); (9) Rodriguez, Tomsick, & Bodaghee (2010); (10) Malizia et al. (2007); (11) Sazonov & Revnivtsev (2004); (12) Reynolds (1997); (13) Rodriguez, Tomsick, & Chaty (2008); (14) Krongold et al. (2009); (15) Terashima et al. (2002); (16) Bauer et al. (2014); (17) Greenhill, Tilak, & Madejski (2008); (18) Malizia et al. (2012); (19) Walton et al. (2014); (20) Parisi et al. (2009); (21) Lewis et al. (2005); (22) Vignali et al. (1998); (23) Revnivtsev et al. (2006); (24) Molina et al. (2009); (25) Vaughan et al. (2004); (26) Walton et al. (2013); (27) Fukazawa et al. (2011); (28) Ikeda, Awaki, & Terashima (2009); (29) Gallo et al. (2006); (30) Revnivtsev et al. (2007); (31) Winter et al. (2008); (32) Immler et al. (2003); (33) Sazonov et al. (2005); (34) Panessa et al. (2008); (35) this work; (36) Risaliti (2002); (37) Sazonov et al. (2008); (38) Eguchi et al. (2011); (39) Comastri et al. (2010); (40) Vignali & Comastri (2002); (41) Landi et al. (2010); (42) Cappi et al. (2006); (43) Turner et al. (2007); (44) Young & Wilson (2004); (45) Shirai et al. (2008); (46) Moran et al. (2005); (47) Braitto et al. (2013); (48) Winter et al. (2009b); (49) Maiolino et al. (1998), strongly variable N_{H} ; (50) Puccetti et al. (2014); (51) Noguchi, Terashima, & Awaki (2009); (52) Vasudevan et al. (2013); (53) Risaliti et al. (2000); (54) Molina et al. (2012); (55) Petrucci et al. (2007); (56) Panessa et al. (2011); (57) Levenson et al. (2001); (58) Landi et al. (2009); (59) Ricci et al. (2010); (60) Malizia et al. (2008); (61) Zhang et al. (2009); (62) Young et al. (2002); (63) Molina et al. (2008); (64) Dewangan & Griffiths (2005); (65) Reeves & Turner (2000); (66) Guainazzi, Matt, & Perola (2005b).

Reynolds C. S., 1997, MNRAS, 286, 513

Ricci C., Beckmann V., Audard M., Courvoisier T. J.-L., 2010, A&A, 518, A47

Risaliti G., Gilli R., Maiolino R., Salvati M., 2000, A&A, 357, 13

Risaliti G., Maiolino R., Salvati M., 1999, ApJ, 522, 157

Risaliti G., 2002, A&A, 386, 379

Rodriguez J., Tomsick J. A., Chaty S., 2008, A&A, 482, 731

Rodriguez J., Tomsick J. A., Bodaghee A., 2010, A&A, 517, A14

Sazonov S. Y., Revnivtsev M. G., 2004, A&A, 423, 469

Sazonov S., Churazov E., Revnivtsev M., Vikhlinin A., Sunyaev R., 2005, A&A, 444, L37

Sazonov S., Revnivtsev M., Krivonos R., Churazov E., Sunyaev R., 2007, A&A, 462, 57

Sazonov S., Revnivtsev M., Burenin R., Churazov E., Sunyaev R., Forman W. R., Murray S. S., 2008, A&A, 487, 509

Sazonov S., Churazov E. M., Krivonos R., Revnivtsev M., Sunyaev R., 2010, Proc. 8th INTEGRAL Workshop "The Restless Gamma-ray Universe", Sept. 27-30 2010, Dublin, id. 6

Sazonov S., et al., 2012, ApJ, 757, 181

Severgnini P., Caccianiga A., Della Ceca R., Braitto V., Vignali C., La Parola V., Moretti A., 2011, A&A, 525, A38

Shirai H., et al., 2008, PASJ, 60, 263

Steffen A. T., Barger A. J., Cowie L. L., Mushotzky R. F.,

- Yang Y., 2003, *ApJ*, 596, L23
- Sunyaev R. A., Titarchuk L. G., 1985, *A&A*, 143, 374
- Terashima Y., Iyomoto N., Ho L. C., Ptak A. F., 2002, *ApJS*, 139, 1
- Treister E., Urry C. M., 2005, *ApJ*, 630, 115
- Turner T. J., Miller L., Reeves J. N., Kraemer S. B., 2007, *A&A*, 475, 121
- Ueda Y., Akiyama M., Ohta K., Miyaji T., 2003, *ApJ*, 598, 886
- Ueda Y., et al., 2007, *ApJ*, 664, L79
- Ueda Y., Akiyama M., Hasinger G., Miyaji T., Watson M. G., 2014, *ApJ*, 786, 104
- Vasudevan R. V., Brandt W. N., Mushotzky R. F., Winter L. M., Baumgartner W. H., Shimizu T. T., Schneider D. P., Nousek J., 2013, *ApJ*, 763, 111
- Vaughan S., Fabian A. C., Ballantyne D. R., De Rosa A., Piro L., Matt G., 2004, *MNRAS*, 351, 193
- Verner D. A., Yakovlev D. G., 1995, *A&AS*, 109, 125
- Verner D. A., Ferland G. J., Korista K. T., Yakovlev D. G., 1996, *ApJ*, 465, 487
- Vignali C., Comastri A., Stirpe G. M., Cappi M., Palumbo G. G. C., Matsuoka M., Malaguti G., Bassani L., 1998, *A&A*, 333, 411
- Vignali C., Comastri A., 2002, *A&A*, 381, 834
- Vignati P., et al., 1999, *A&A*, 349, L57
- Walton D. J., Nardini E., Fabian A. C., Gallo L. C., Reis R. C., 2013, *MNRAS*, 428, 2901
- Walton D. J., et al., 2014, *ApJ*, 788, 76
- Winter L. M., Mushotzky R. F., Tueller J., Markwardt C., 2008, *ApJ*, 674, 686
- Winter L. M., Mushotzky R. F., Reynolds C. S., Tueller J., 2009a, *ApJ*, 690, 1322
- Winter L. M., Mushotzky R. F., Terashima Y., Ueda Y., 2009b, *ApJ*, 701, 1644
- Young A. J., Wilson A. S., Terashima Y., Arnaud K. A., Smith D. A., 2002, *ApJ*, 564, 176
- Yaqoob T., 2012, *MNRAS*, 423, 3360
- Young A. J., Wilson A. S., 2004, *ApJ*, 601, 133
- Zhang S., Chen Y. P., Torres D. F., Wang J. M., Li T. P., Ge J. Q., 2009, *A&A*, 505, 553